Complete Title: A Comparison of Solidification Structures and Sub-Microscale Cellular Segregation in Rapidly Solidified Stainless Steels Produced via Two-Piston Splat Quenching and Laser Powder Bed Fusion

Brief Title: Characterization and comparison of Two-Piston Splat Quenching vs. Laser Powder Bed Fusion 316L Stainless Steel

Authors: Zachary Arthur Hasenbusch (a,), Andrew Deal (b), Ben Brown (b), Davis Wilson (b,1), Laurentiu Nastac (a), Luke N. Brewer (a)

Affiliation:

a. Metallurgical and Materials Engineering, The University of Alabama, Tuscaloosa, AL, 35487, United States **(Primary Institution)**

b. Department of Energy's National Security Campus, Honeywell Federal Manufacturing & Technologies, Kansas City, Missouri, USA 14520 Botts Road, Kansas City, MO, 64147 United States

Corresponding Author: Z. A. Hasenbusch,

Competing interests: The author(s) declare none

UUR
NSC-614-4970
March 2023

Abstract

Fusion-based additive manufacturing techniques leverage rapid solidification (RS) conditions to create parts with complex geometries, unique micro/nanoscale morphological features, and elemental segregation. Three custom composition stainless steel alloys with varying chrome equivalence to nickel equivalence ratio (Cr/Ni_{eq}) between 1.53 and 1.95 were processed using laser powder bed fusion (LPBF) and/or two-piston splat quenching (SQ) to produce solidification rates estimated between 0.4-0.8 m/s. Both SEM and TEM were utilized to collect high-resolution images, electron backscatter diffraction (EBSD) phase identification, and measure cellular segregation in various RS microstructures. Similar features were observed in both LPBF and SQ samples including phase and microstructure, nanoscale oxide particles, cell size, and segregation behavior. However, dislocation pileup was observed along the cell boundaries only in the LPBF austenite solidified microstructure. Targeted adjustment of the SQ feedstocks Cr and Ni concentrations, within the ASTM A240 316L specification for 316L, resulted in no observable impact on the cell size, oxide particle size, or magnitude of segregation. Also, the amount of Ni segregation in the ferrite solidified microstructures did not significantly differ, regardless of Cr/Ni_{eq} or processing technique. SQ is demonstrated as capable of simulating RS rates and microstructures similar to LPBF for use as an alternative screening tool for new RS alloy compositions.

1. Introduction

Powder bed fusion (PBF) processing techniques rely heavily on rapid solidification (RS) to create parts with complex geometries that would not be feasible through traditional production processes. Austenitic stainless steels are commonly used in PBF processing with great success to create high strength parts with good corrosion resistance and thermo-mechanical properties. (Bartolomeu, et al., 2017; Cheruvathur, et al., 2015) These properties are achieved partially as a result of the unique micro and sub-microstructures formed by rapid solidification (RS). (Akbari & Kovacevic, 2018; DebRoy, et al., 2018; Deng, et al., 2020; Qiu, et al., 2018; Wang, et al., 2018) Cooling rates and solidification rates experienced during PBF processing can vary extensively based on the material and build parameters, for example, stainless steels processed via laser powder bed fusion (LPBF) can achieve cooling rates between 10^3 and 10^7 K/s. (Bertoli, et al., 2019; DebRoy, et al., 2018; Kong, et al., 2019a; Kong, et al., 2019b; Sun, et al., 2016) However, the relationship between composition, microstructure, and rapid solidification is not fully understood, so before new alloys can be used, they must be investigated to ensure the desired properties will be achieved after RS. (Bartolomeu, et al., 2017; Kürnsteiner, et al., 2017; Tchuindjang, et al., 2017) The metallic powder used in PBF processes requires specialized equipment to make, can cost thousands of dollars to purchase in sufficient quantities for PBF, and generate waste from required size distributions that are necessary for consistent and quality results. Also, the PBF equipment must be emptied and cleaned when changing alloy compositions. These factors make testing new alloy compositions a costly and time-consuming processes.

RS that occurs during fusion-based additive manufacturing (FBAM) processes such as PBF, enables the formation of unique micro and sub-microscale structure and features in stainless steels. RS conditions are generally considered to be achieved at solidification rates above 10 mm/s or cooling rates above 100 K/s. (Elmer, 1988; J. A. Sarreal, 1986; Kurz & Trivedi, 1994) Most FBAM stainless steels are characterized by the cellular solidification structures that can form as a result of RS. solidification structure can be observed by etching a polished cross section, or by using TEM bright field (BF) imaging. In BF images of 316L, the solidification structure is outlined by networks of dislocations along the cell boundaries.(Bajaj, et al., 2020) The dislocation networks result in a sub-structure within the microstructure. (Bajaj, et al., 2020; Gao, et al., 2020; Jacob, 2018; Liu, et al., 2018; Voisin, et al., 2021; Voisin, et al., 2018; Wang, et al., 2018; Wilson, 2019) Along with the dislocation pileup, nanoscale oxide particles have also been found along the cell boundaries.(Bajaj, et al., 2020; Liu, et al., 2020; Liu, et al., 2018; Voisin, et al., 2021; Wang, et al., 2018; Wilson, 2019) These oxide particles were identified as Mn enriched Si oxides, or Rhodonite ($MnSiO_3$) and have been found to range in size between 10 and 300 nm. (Bajaj, et al., 2020; Gorsse, et al., 2017; Qiu, et al., 2018; Wang, et al., 2018; Yan, et al., 2018) In some studies, other Cr-rich oxides have also been reported, but these were not found as frequently. (Deng, et al., 2020; Qiu, et al., 2018) The MnSi oxides are reported to act as Zener pinning sites at the cell boundaries for the dislocation pile up and are partially responsible for the improved material properties. (Deng, et al., 2020; Yan, et al., 2018) In rapidly solidified austenitic stainless steels the segregation of Cr, and if present, Mo to the cell boundaries has been repeatedly reported. (Deng, et al., 2020; Voisin, et al., 2018; Wang, et al., 2018; Wilson, 2019) The segregation of these heavy elements to cell boundaries has also been suggested to contribute to improved material properties. (Deng, et al., 2020; Voisin, et al., 2021; Wang, et al., 2018) The ability of RS processing to produce microstructures and features that are distinctly different from what occurs at slower solidification rates creates an opportunity for current metallic systems to be implemented in new ways.

Rapid solidification is known to affect the resultant phase/microstructure formed at certain compositions in austenitic stainless steels and, in some cases, this deviation from the equilibrium predicted microstructure can significantly impact the properties of the final product. Stainless steel and RS literature use the concept of equivalence equations, such as WRC-1992, to quantitatively represent a materials tendency to form either austenite or ferrite microstructures based on the chemical composition. (Elmer & Eagar, 1988; Elmer, et al., 1989; Elmer, et al., 1990; Lippold, 1994; Lippold & Savage, 1979; Lippold & Savage, 1980; Schulz, 2020; Wilson, 2019) The WRC-1992 equations have undergone significant evaluation and review to confirm the accuracy of the predictions and have been shown to have a wide range of applications from estimating ferrite content in dissimilar metal welds to predicting microstructures and material properties for stainless steels. (Kotecki & Siewert, 1992) The equations are used to calculate what are referred to as chrome equivalence (Cr_{eq}) and a nickel equivalence (Ni_{eq}) values to indicate the materials tendency to form either ferrite or austenite respectively. A ratio of the Cr_{eq} and Ni_{eq} (Cr/Ni_{eq}) can also be taken and used in a similar manner. Higher solidification rates have been found to increase the range of equivalence values over which austenite and ferrite solidification was stable, reducing the predicted two-phase region. (Stefanescu, 2002) Rapid solidification rates tend to produce single phase solidification of either austenite or ferrite, typically resulting in three possible microstructures; primary austenite (PA) from austenite solidification, primary ferrite (PF) from ferrite solidification, and austenite formed from a solid-state massive transformation of ferrite

(F/MA). (Elmer, et al., 1989; Lippold, 1994) While the WRC-1992 equations were developed with respect to techniques like arc welding that had slower solidification rates than RS, the equations are still able to provide a foundation of what would be expected from the steel at slower solidification rates and allows for a better understanding of how that has changed at higher solidification rates. Separate works by Jacob and Lippold each demonstrate the use of WRC-1992 equivalence ratios being used to compare stainless steels of different composition for RS processes like pulsed laser welding and LPBF. (Jacob, 2018; Lippold, 1994) The effect of RS on the ranges of equivalence values over which these microstructures form is critical to understand when performing FBAM processes in order to ensure the desired material properties in the finished part.

In slower, non-rapid solidification rate processes, such as arc welding of austenitic stainless steel, dendritic solidification will occur along with elemental segregation. During austenitic soldificaiton, Cr and Ni exhibit an inverse segregation behavior in which Cr becomes enriched at dendrite boundaries and depleted at the dendrite core, and Ni enriched at the dendrite core and depleted along the dendrite boundaries. (Brooks, et al., 1991; Brooks & Thompson, 1991; Mas, et al., 2018) The opposite segregation response was observed in ferritic microstructures in which there was Ni enrichment at boundaries and Cr at cell centers. This difference in elemental segregation in which Cr is rejected during austenite solidification and Ni is rejected during ferrite solidification is explained by Cr being a ferrite stabilizer and Ni being an austenite stabilizer. (Kou, 2002) This type of segregation is under the assumption of the limited diffusion in the liquid with no solid diffusion model. The segregation at the dendrite core is referred to as an initial transient region and the segregation at the dendrite boundary is the final transient region. In welding and FBAM processes that experience rapid solidification rates, the solidification morphologly will typically be cellular and can produce microscale cellular segregation. When electron beam welding was used, which has a much higher solidification rate, the initial transient region was no longer observed but the final transient region remained. (Brooks, et al., 1991; Brooks & Thompson, 1991; Iamboliev, et al., 2003) In a different study of austenitic 316L, produced by LPBF in which the solidification rates are higher than conventional arc welding, the enrichment of Cr, Ni, Mo, and Mn was reported at the cell boundaries with no observable change in composition within the cell body. (Gorsse, et al., 2017) Similarly, in LPBF processed austenitic 316L material, Voisin et. al. reported both Cr and Mo segregation to the cell boundaries. (Voisin, et al., 2021) This study did not mention the Ni or Mn response at the cell boundaries. The variation in reported segregation profiles found in rapidly solidified stainless steels further highlights the need for a better understanding of how RS changes solidification microstructures in various processing methods.

Along with micro-segregation, the possibility of solid-state diffusion (SSD) after solidification has been previously proposed. During separate studies by Brooks and Iamboliev, they reported rapidly solidified ferritic structures in which cell boundaries were homogenous after solidification and SSD was used to explain the resulting lack of observed segregation at the RS cell boundaries. (Brooks, et al., 1991; Brooks & Thompson, 1991; Iamboliev, et al., 2003) There are multiple factors that can impact whether SSD will occur, such as crystal structure, element, distance, and temperature. The amount of SSD that can occur in a solidified material will change based on the phase, as the diffusion properties of elements is different in austenite vs ferrite. (Brooks, et al., 1991; Iamboliev, et al., 2003; Wilson, 2019) Also, whether SSD will occur or to what degree is dependent on the processing technique and conditions, as sufficient time and temperature are required. Although, micro-segregation in rapidly solidified stainless steel has been reported in the solidified microstructures, the possibility that the observed segregation has been modified by SSD must also be considered.

Several solidification models have been developed and or modified to simulate rapid solidification conditions more accurately using correction factors or by incorporating phenomena such as solid-liquid boundary diffusion and solute trapping. At equilibrium solidification rates, tools such as phase diagrams and the lever rule generally predict solidification segregation well. More complex, non-equilibrium solidification models, such as Scheil, are useful for simulations at intermediate solidification velocities and can produce first order estimates for the low end of rapid solidification. (Cheruvathur, et al., 2015) As solidification rates increase, prior assumptions about diffusion and interface kinetics are no longer accurate requiring velocity corrected models such as the continuous growth model presented by Aziz. (Aziz, 1982; ThermoCalc, 2021) These typically combine models addressing effects such as undercooling, dendrite tip radius, and the absolute limit of stability with larger models to improve results. (Kurz & Fisher, 1981; Kurz, et al., 1986; Kurz & Trivedi, 1994; Lipton, et al., 1987; Trivedi & Kurz, 1994; Trivedi, et al., 1987) Additionally, to validate these models, a more comprehensive understanding of rapid solidification for stainless steels may well require the study of many, different alloy compositions which span the microstructure space from PA – F/MA – PF. To do so, will require an efficient means of producing a variety of stainless steels, performing rapid solidification experiments, and characterizing the result RS microstructure.

Two-piston splat quenching (SQ) is a useful tool for generating samples with RS rates similar to PBF processes. The technique requires very little feedstock (<1 gram) to perform experiments, feedstock does not need to be in powder form, and experiments can be completed from start to finish in a matter of a couple hours. By comparison, a standard LPBF build process requires several kilograms of powder to be produced by a series of atomization experiments and subsequent powder sizing and characterization, costing significantly more time and capital. The SQ process utilizes rapid solidification to create thin foils with high cooling rates and cellular solidification structures. (Inokuti & Cantor, 1977) SQ is capable of achieving cooling rates beginning around 10^4 K/s and increasing up to 10^8 K/s or higher under the right circumstances. (Jones, 1996; Jones & Suryanarayana, 1973; Prakash, et al., 1992; Predecki, et al., 1965; Quintana, et al., 1979; R. W. Cahn, 1976; Ruhl, 1967; Ruhl & Cohen, 1969; Scott, 1975; Wood & Honeycombe, 1974) Such a wide range in cooling rates is achievable through targeted modification of key experimental parameters such as sample size, surface roughness, and platen material. (Jones, 1996; Jones & Suryanarayana, 1973; Prakash, et al., 1992; Ruhl, 1967; Ruhl & Cohen, 1969)

This paper compares the RS microstructures produced by LPBF and SQ experiments using a variety of custom stainless steel alloys which span the microstructure space between PA, F/MA, and PF. The solidified materials were examined using a combination of micro and nanoscale analysis techniques to assess microstructure, solidified phase, elemental segregation, and micro/nanostructural features. Unlike in previous works, this paper discusses the similarities and differences between microstructures for a single alloy chemistry produced with two unique rapid solidification processes and investigates the potential relationship between the Cr/Ni_{eq} and elemental segregation in multiple alloys and microstructures produced by SQ. Detailed imaging using scanning electron microscopy (SEM), transmission electron microscopy (TEM), scanning transmission electron microscopy high-angle annular dark-field (STEM-HAADF) was performed, and analysis using electron backscatter diffraction (EBSD) and STEM energy dispersive X-ray spectroscopy (EDX) measurement techniques were implemented to examine the samples at the micro and nanoscales. In addition, segregation ratios estimated from the experimental results were compared to segregation ratios from simulated solidification using both classic Schiel solidification and Scheil with solute trapping modules in Thermo-Calc. Finally, this paper demonstrates that the SQ technique can be used as an effective means to efficiently explore the RS microstructure space similar to LPBF for stainless steels.

2. Materials and Methods

2.1 Alloy production and rapid solidification processing.

A total of three different alloy compositions were produced in this investigation that had increasing Cr/Ni$_{eq}$ ratios of 1.53, 1.71, and 1.95 using the WRC 1992 equivalence equations. (Kotecki & Siewert, 1992) Alloy 1 was a 316L type stainless steel that was within the ASTM-A240 composition specification had been processed via LPBF. (ASTM, 2020) Alloys 2 and 3 were produced using high purity raw material that was arc melted together to achieve homogenous feedstock with the targeted chemistries. All raw material purities were 3N or higher. Iron was in the form of 1/8” pellets and Cr sputtering targets were used for alloying while the rest of the material was in powder form and pressed into a pellet. Alloy compositions were measured after arc melting and rolling using the following bulk chemical analysis techniques: inductively coupled plasma optical emission spectroscopy, combustion analysis, and inert gas fusion. A portion of the LPBF material was sectioned and used for SQ experiments of that alloy composition. Three replicate samples were made from each alloy composition using SQ. SQ was performed in an ultra high purity Ar environment. For the SQ experiments, the samples were electromagnetically levitated, melted, and brought to a target temperature of 1600°C before being released and splatted between two Cu platens to create the thin foils.

2.2 Sample preparation.

To prepare samples for analysis both SQ and LPBF samples were cross sectioned and mounted in the electrolytically conductive hot mount material, PolyFast. The LPBF sample was cut through the middle to expose melt pool cross sections. SQ produced thin foil samples were sectioned longitudinally through the middle, as if cutting a coin in half, and mounted with the cross section exposed. All mounted samples were ground and polished to a 1µm finish then either electrolytically etched in a 60/40 solution of 70% nitric acid and deionized (DI) water using a DC power supply at 1.25 V to reveal solidification microstructure, or vibratory polished using 0.02µm solution for EBSD.

TEM foils were made via focused ion beam (FIB) lift outs from etched samples. FIB lift outs were performed using either a TESCAN LYRA FIB-FESEM or FEI Quanta 3D Dual Beam, both of which use a gallium ion source. First a region of interest was identified, in which a group of cells were aligned and in-plane. In splat quenched samples this was within the radial center of the splat quench. For LPBF material the region of interest was within the interior of the build away from any edges. The FIB was used to deposit a bar of platinum perpendicular to the orientation of the solidification cells to produce a cross section of the cells when viewed in the TEM. The TEM foil was then cut and lifted out from the sample and attached to a Cu grid. The foil was thinned until a thickness was 150 nm or less was achieved.

2.3 SEM imaging and EBSD.

An SEM was employed for high-resolution imaging of the etched cell structure and to perform EBSD analysis of polished samples. Images were collected on a Thermo-Fisher Apreo SEM while EBSD was completed using a JEOL 7000 SEM and the software Aztec produced by Oxford. SEM images and EBSD scans of SQ material were collected from the radial center of the samples. Images and EBSD scans of LPBF material were from the interior of the sample build. All TEM and STEM work was performed on an FEI TECNAI F-20 microscope at 200 kV. BF and STEM-HAADF images were collected using the GMS III software and images were collected at a range of camera lengths.

2.4 Cell size measurement and solidification rate estimates.

Cell diameters were measured using a combination of SEM images of the etched microstructure and ImageJ software. Multiple sets of cell size measurements were collected from both the LPBF and SQ samples. Cooling rates were estimated based on the range of cell sizes measured using an empirical relationship proposed in work by Katayama et. al. for 310 SS in which D is the cell size, R is the cooling rate, and A and n were material constants, 80 and 0.38 respectively. (Katayama & Matsunawa, 1984)

$$D=A*(R)^{-n} \qquad \text{Equation 2.4.1}$$

To solve for the solidification rate, the cooling rate was divided by temperatures gradients that were extracted from 2-D ANSYS heat transfer simulations of the solidification event. The simulation used a heat transfer coefficient of h=1E7 W/m^{2}K and a solidification temperature range of 40K. (Katayama & Matsunawa, 1984; Zacharia, et al., 1989)

2.5 ThermoCalc simulations.

The thermodynamic modeling software Thermo-Calc 2022a was used to run multiple solidification models for each alloy feedstock composition being studied. Simulations were performed using the classic Scheil solidification module (Equation 2.5.1) in which C_S is the composition of the solid, k_{eq} is the equilibrium partition coefficient, C_0 is the initial composition, and f_S is the fraction solid. (Kou, 2002)

$$C_s = k_{eq} * C_0 * (1 - f_s)^{k_{eq}-1} \qquad \text{Equation 2.5.1}$$

The velocity modified Scheil with solute trapping module was also used to perform solute trapping simulations at three different rapid solidification rates 0.1 m/s, 1.0 m/s, and 5.0 m/s. All simulations were completed using the TCFE8 Steels/Fe-alloys database. The allowed phases in each simulation were restricted to only the liquid phase and the observed primary solidification phase of that alloy. This was done to account for the change in primary solidification phase caused by rapid solidification and to reflect what was observed in the experimental results. The classic Scheil and Scheil with solute trapping model were ran to 95% completion. The Scheil with solute trapping module is based on previous work by Aziz and Jackson that presented an equation for a velocity corrected partition coefficient shown in Equation 2.5.2. (Aziz, 1982; Boettinger, et al., 1984; ThermoCalc, 2021)

$$\mathrm{k_V} = \frac{k_{\mathrm{eq}} + \beta_0 * V}{1 + \beta_0 * V} \qquad \text{Equation 2.5.2}$$

In this equation, k_V is the velocity corrected partition coefficient, k_{eq} is the equilibrium partition coefficient, V is the solidification front velocity, and β_0 I s a ratio between the interatomic distance length scale and diffusion coefficient. This ThermoCalc model solves for the partitioning coefficient at each step under increased solidification rates.

2.6 STEM-EDX line scan and analysis.

STEM-EDX line scans were collected from TEM foils using a single tilt, low background beryllium sample holder. STEM-EDX was performed using an EDAX Optima-T-60 windowless detector and analyzed using the EDAX-TEAM software. To assess overall variation of the concentration of each element across individual solidification cells, a ratio of element signal intensity vs Fe was used to account for and remove any variation in signal intensity caused by changes in sample thickness. However, this method does not differentiate between changes in the individual element signal intensity vs changes in the Fe signal intensity, both of which can shift the ratio of signal intensities. As a result, this method was only used to qualitatively analyze the change in signal intensity over the course of the line scan data.

2.7 Segregation ratio and solid-state diffusion calculations.

The partition coefficient, k_{eq}, is commonly presented as shown in Equation 2.7.1, in which C_S is the concentration of an element present in the solid, and C_L is the concentration of the same element in the liquid.

$$k_{eq} = \frac{C_S}{C_L} \qquad \text{Equation 2.7.1}$$

For equilibrium and near equilibrium solidification conditions, C_L can be replaced with the concentration of the respective element in the final solid to solidify. However, under rapid solidification conditions when solving for the partition coefficient, C_L can not be replaced with the concentration in the final solid due to phenomena like undercooling, cell tip radius, and diffusion in the liquid and solid to name a few. Instead, the ratio of initial vs final concentration that was previously the partition coefficient, now is the segregation ratio.

In order to quantify the amount of segregation, segregation ratios were measured using experimental data from multiple cells in each microstructure and compared with thermodynamic simulations. When calculating the segregation ratio from solidification simulations C_S was the initial composition and C_L was the final composition of the solidified phase. For the experimental data, integrated and background subtracted X-ray signal intensities from individual line scans were used to represent individual element concentrations. This was done because of difficulties associated with precisely and accurately converting STEM-EDX data into elemental compositions for complex alloys. The average signal intensity from the cell center was used as C_S and the signal intensity at the cell boundary was C_L. In cases where individual element signal intensity was skewed by variations in foil thickness, the ratio of signal intensities data was used to identify the location of the cell boundary and the start of the segregation and in which the signal intensity stabilized, and these values were used. The segregation ratio was not calculated using the ratio of individual element signal intensity vs Fe signal in order to provide a more accurate representation of the segregation of each individual element.

Fick’s law of diffusion was used to estimate SSD distances for the LPBF and SQ processes. Equation 2.7.2 shows Fick’s law of diffusion in which D is the diffusion coefficient, D_0 is a temperature-independent pre-exponential constant, Q is the activation energy, T is temperature, and R is the gas constant.

$$D = D_0 * \exp\left(\frac{-Q}{RT}\right) \qquad \text{Equation 2.7.2}$$

Values for D_0 and Q for Cr and Ni were selected from work by Brooks et. al., and D was solved for temperature values between the 1410°C and the estimated transformation temperature 1350°C. (Brooks, et al., 1991) Three potential diffusion times were used in diffusion distance calculations that were based on cooling rate estimates from cell size measurements, 1E-4, 1E-5, and 1E-6 seconds.

3. Results

3.1 Microstructures and cellular morphology.

The three stainless steel alloys used in this study had similar compositions that spanned a range of Cr/Ni_{eq} values from 1.53 to 1.95 through varied Cr, Ni, and Mo concentrations. The measured individual alloy compositions are listed in Table 3.1.1 along with the WRC-1992 equivalence values and Cr/Ni_{eq} ratios for each alloy. Alloys 1 and 2 were within the ASTM A240 compositional specification for 316L SS which defines a range of allowable concentrations for Cr, Ni, and Mo. Alloy 3 almost met the specification, but contained 0.1 wt% Cr more than allowed for 316L SS. The only other major compositional difference between the alloys was that the concentration of C in alloy 1 was an order of magnitude greater than in alloys 2 and 3, but still below the 0.03 wt% upper limit for low carbon SS. Alloys 2 and 3 had lower C contents than alloy

1 because they were custom alloys made using high purity raw elements and alloy 1 was supplied for the study.

Table 3.1.1. Measured bulk chemistry analysis results for feedstock alloys 1-3 with equivalence values.

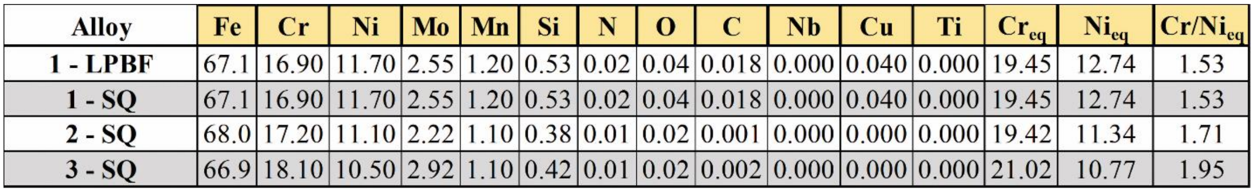

Alloy	Fe	Cr	Ni	Mo	Mn	Si	N	O	C	Nb	Cu	Ti	Cr_{eq}	Ni_{eq}	Cr/Ni_{eq}
1 - LPBF	67.1	16.90	11.70	2.55	1.20	0.53	0.02	0.04	0.018	0.000	0.040	0.000	19.45	12.74	1.53
1 - SQ	67.1	16.90	11.70	2.55	1.20	0.53	0.02	0.04	0.018	0.000	0.040	0.000	19.45	12.74	1.53
2 - SQ	68.0	17.20	11.10	2.22	1.10	0.38	0.01	0.02	0.001	0.000	0.000	0.000	19.42	11.34	1.71
3 - SQ	66.9	18.10	10.50	2.92	1.10	0.42	0.01	0.02	0.002	0.000	0.000	0.000	21.02	10.77	1.95

EBSD phase mapping was used to identify austenite and ferrite phases in the rapidly solidified samples produced by LPBF and SQ processing. Alloy 1 samples that were processed using LPBF and SQ both produced fully austenitic microstructures. A fully austenitic microstructure was also observed in the SQ alloy 2 samples at and around the radial center with a few, very small pieces of ferrite were found near the outter radial edges of the sample. It should be noted that the PA and F/MA microstructures are both crystallographically austenite and can not easily be distinguished when in EBSD. In the EBSD phase map of alloy 3, both austenite and ferrite were found in significant amounts. (Figure 3.1.1D) Figure 3.1.1A-D contains phase maps for each of the four samples in which blue is austenite and red is ferrite. In Figures 3.1.1A-C, small amounts of ferrite are indicated at the grain boundaries of the austenitic material. This was due to low quality Kikuchi patterns generated at the grain boundaries that were mis-indexed by the software and can be ignored.

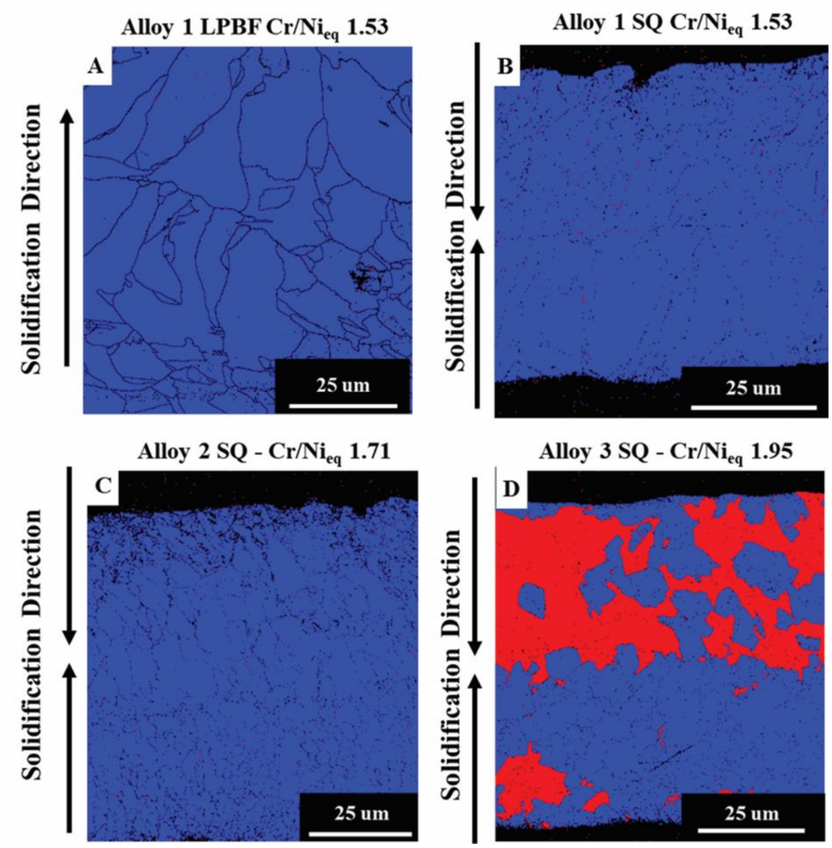

Figure 3.1.1. EBSD Phase maps from (A) build center of LPBF alloy 1 and (B-D) from radial center of SQ alloys, 1-3 respectively. Blue represents austenite and red represents ferrite.

Electrolytic etching exposed the cellular solidification structure of each sample and also used to differentiate the PA microstructure from F/MA or PF microstructures. Two distinctly different cell types were observed after etching. Type 1 cells were identified by the preferential etching response at the cell boundary while the body of the cell remained mostly unaffected. Type 2 cells were characterized by an overall less defined etching response under the same conditions, with cell boundaries being etched less preferentially to the cell body compared to type 1 cells. Examples of the two cell types can be found in Figure 3.1.2A-H. Type 1 cells were identified to have formed from austenite material that experienced austenitic solidification. PF and F/MA microstructures both formed type 2 cells as a result of the ferritic solidification. Previous work by S. Venkataraman shows examples of primary austenite cell structures (type 1) and cell structures from the ferrite to austenite transformed material (type 2) in 316L stainless steel. (Venkataraman, 1984) While it was observed in EBSD phase maps that LPBF and SQ alloy 1 were fully austenitic, both type 1 and 2 cells could be distinguished in the samples after etching. (Figure 3.1.2A-D) In LPBF alloy 1, type 1 cells consistently formed along the bottom edge of the weld pool and type 2 cells formed closer to the interior/top of the weld pool. In the corresponding SQ sample from alloy 1, type 1 cells were typically observed along the PS interface while type 2 cells were found more commonly in the middle in which the two solidification fronts meet. In both processing techniques of the alloy 1 composition, type 1 cells were found in areas in which cooling rates and solidification rates were predicted to be the fastest and type 2 cells in the areas in which lower cooling and solidification rates were expected. Unlike in alloy 1, alloys 2 and 3 formed only type 2 cells regardless of if the sample indexed as austenite or ferrite in EBSD. The cellular structures for these two samples are shown in Figure 3.1.2E-H.

The cell size measurements showed a larger average cell size for LPBF processed material compared to in the SQ sample but overall, the two processes both produced solidification cells between 0.20 and 0.40 µm in diameter. This range of cell sizes translated to cooling rate estimates between $9.3*10^6 – 7.7*10^7$ K/s based on the empirical relationship discussed earlier. Solidification rate estimates using the extracted temperature gradients and cooling rate estimates were between ~390 mm/s and 830 mm/s. The cell sizes measured from SQ alloy 2 and alloy 3 were similar in magnitude to the cell size measurements of SQ alloy 1. In order to achieve a more detailed comparison of the nanostructural features between samples, TEM and STEM analysis of both type

1 and type 2 cells from LPBF and SQ samples of alloy 1, type 2 cells from F/MA in alloy 2, and type 2 cells from PF in alloy 3 were performed.

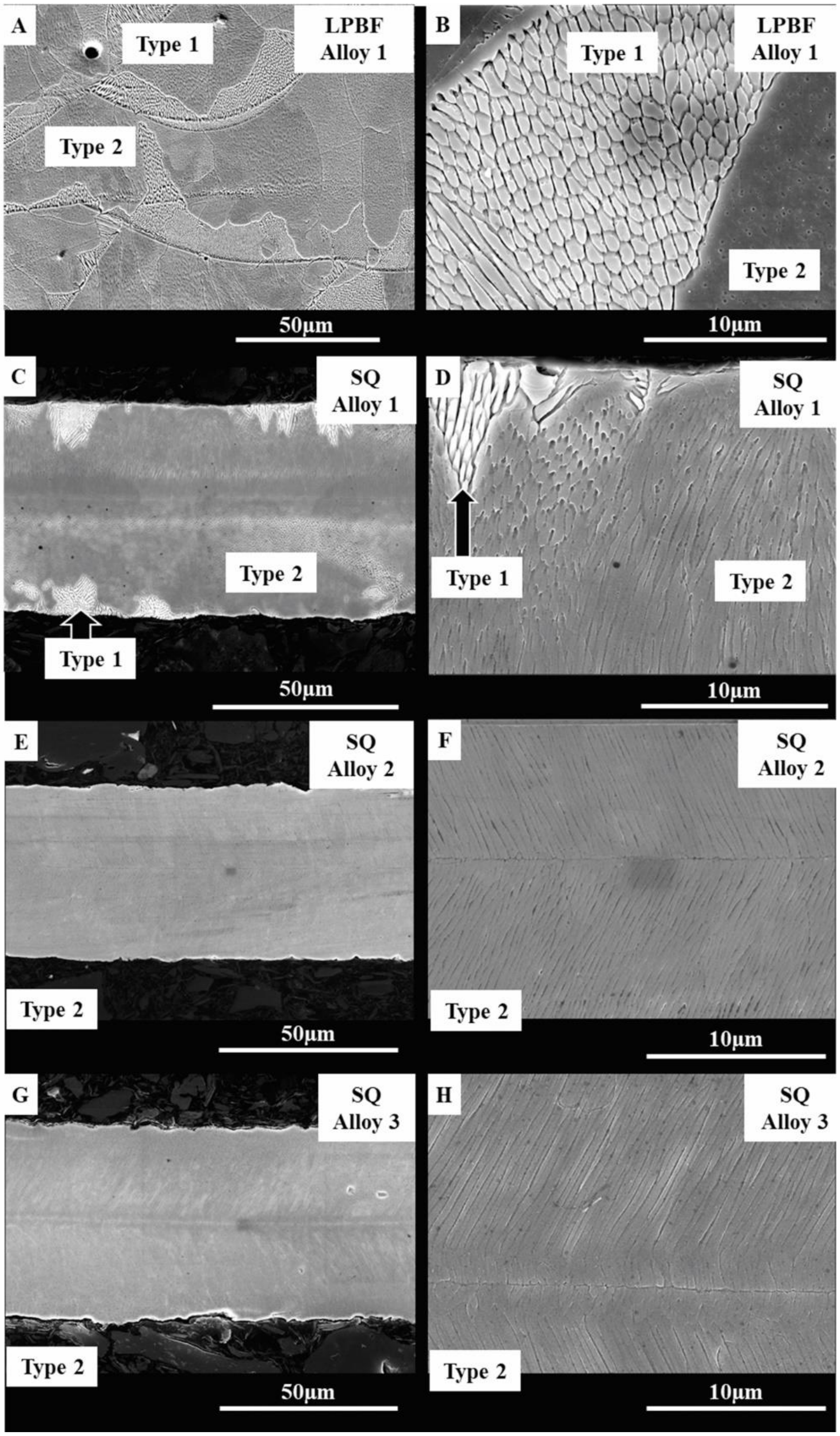
A
Type 1
LPBF
Alloy 1
Type 2
50µm
B
Type 1
LPBF
Alloy 1
Type 2
10µm
C
SQ
Alloy 1
Type 2
Type 1
50µm
D
SQ
Alloy 1
Type 1
Type 2
10µm
E
SQ
Alloy 2
Type 2
50µm
F
SQ
Alloy 2
Type 2
10µm
G
SQ
Alloy 3
Type 2
50µm
H
SQ
Alloy 3
Type 2
10µm

Figure 3.1.2. Low and high magnification SEM images of type 1 (austenite solidification) and type 2 (ferrite solidification) cells observed in: (A, B) LPBF alloy 1, (C, D) SQ alloy 1, (E, F) SQ alloy 2, (G, H) SQ alloy 3.

3.2 TEM and STEM-HAADF images.

BF and STEM-HAADF imaging of PA in LPBF and SQ samples revealed mostly similar micro and sub-microscale structures and features between the two processing methods. The cellular solidification structures were easily observable in BF and STEM-HAADF images of the PA, type 1 cells from LPBF produced alloy 1. The cell boundaries were identified in BF by the dislocation pileup at the cell boundaries, which could also be seen in the STEM-HAADF images, Figure 3.2.1A-D. This type of dislocation buildup along the cell boundaries is characteristic of LPBF and other PBF processed austenitic stainless steels. In addition to the dislocation pileup, a network of oxide particles could also be observed that formed along the cell boundaries. The oxide network was most easily observed in the STEM-HAADF images but could be observed in BF images by over or under focusing the image. In Figure 3.2.1B, the image was intentionally under-focused to make the oxides more visible through the dislocation pileup. Cell boundaries were not always constrained by grain boundaries and were found across and along grain boundaries. The size of the oxides formed in this material ranged from ~5 nm in diameter at the smallest to ~100 nm in diameter for the larger oxides. Oxide particles were found primarily along the cell boundaries and sometimes at grain boundaries but not all of the time.

The PA, type 1 cells produced by SQ in alloy 1 were similar to the PA from the LPBF material but exhibited smaller oxide particles and lacked the dislocation pileup observed in LPBF.

The SQ PA sample formed a similar oxide network along the cell boundaries, like in the LPBF material, that was visible in both BF and STEM-HAADF images. (Figure 3.2.2) Unlike the LPBF sample, no dislocation pileup at the cell boundaries was observed in SQ PA material. Although, under-focusing the BF image was still required to observe the oxides. The oxide particles that formed in the PA SQ material did not form as large as in the LPBF PA, only ranging from ~5nm to ~30 nm in diameter. The oxides in SQ PA were found along cell boundaries and at grain boundaries when they were the same. While SQ PA exhibited cellular solidification and a network of oxides along the cell boundaries similar to LPBF, the oxide particles formed were not as large, and no observable dislocation pileup along the cell boundaries are what features differed between the PA microstructures formed by LPBF and SQ.

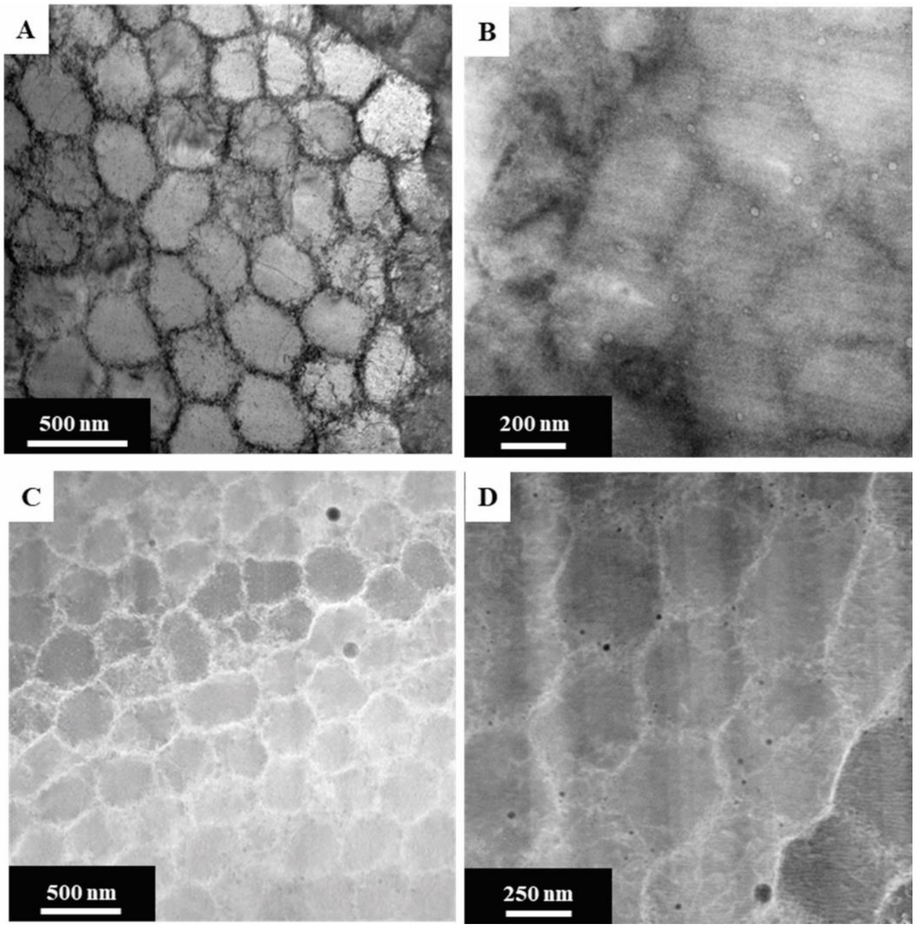

Figure 3.2.1. PA microstructure (type 1 cells) in alloy 1 produced by LPBF. (A-B) TEM-BF images and (C-D) STEM-HAADF images. Image B and D are higher magnification to show detail that is difficult to resolve at lower magnification. Image B was intentionally under-focused to make oxides more visible through dislocation pile-up.

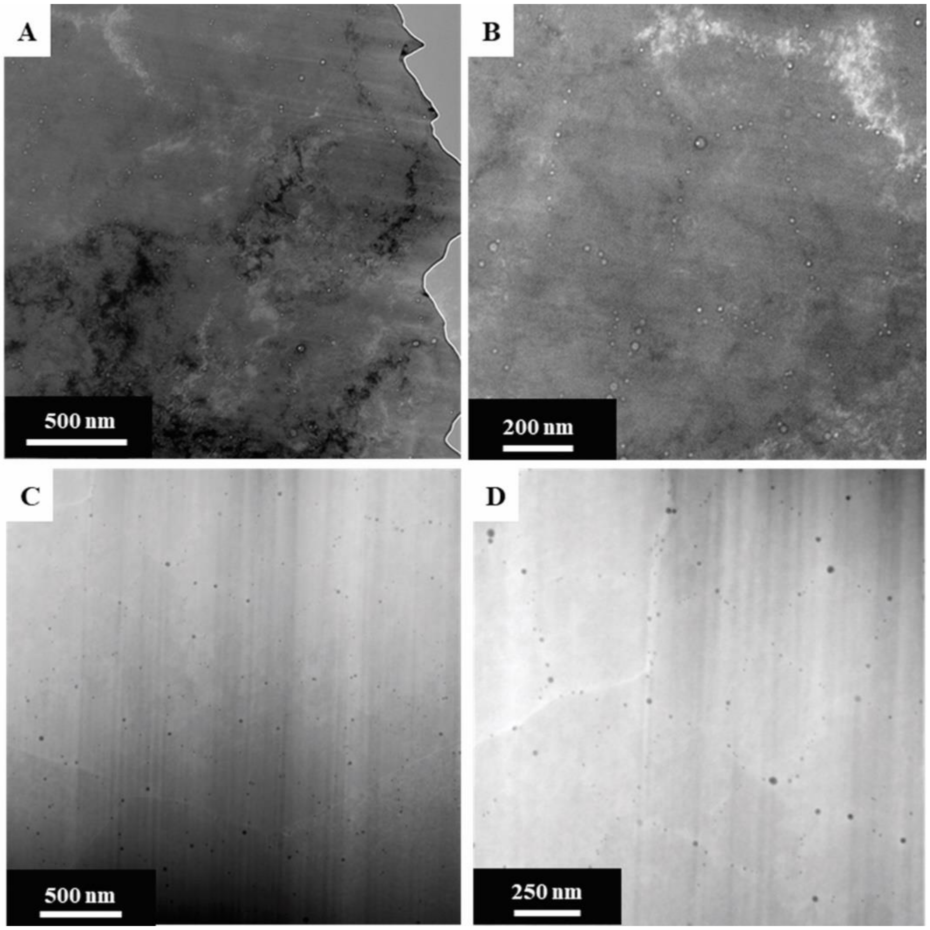

Figure 3.2.2. PA microstructure (type 1 cells) in alloy 1 produced by SQ. (A-B) TEM-BF images and (C-D) STEM-HAADF images. Image B and D are higher magnification to show detail that is difficult to resolve at lower magnification. Images A and B were intentionally under-focused to make oxides more visible.

BF and STEM-HAADF images of the F/MA microstructure, type 2 cells from LPBF and SQ alloy 1 were more similar than the PA microstructures, in which the only difference was how large of oxide particles formed in the LPBF vs SQ material. The network of oxides was observable in the F/MA samples from both LPBF and SQ material. As described earlier, the oxide network that outlined the cell boundaries was observed in STEM-HAADF images normally and BF images more easily by under-focusing the image. (Figure 3.2.3A-D) Unlike in the LPBF produced PA, dislocation pileup at the cell boundaries was not observed LPBF produced F/MA samples. The oxides that formed in the LPBF F/MA material were similar in size to what was observed in PA, ~5 to ~100 nm in diameter. The same was true for SQ F/MA in which the oxides ranged from ~5 to ~30 nm. The F/MA microstructures in LPBF and SQ processed alloy 1 were more similar than the PA microstructures since no dislocation pileup was observed in either sample, however, the size range of oxides in the LPBF material was still larger than in the SQ material.

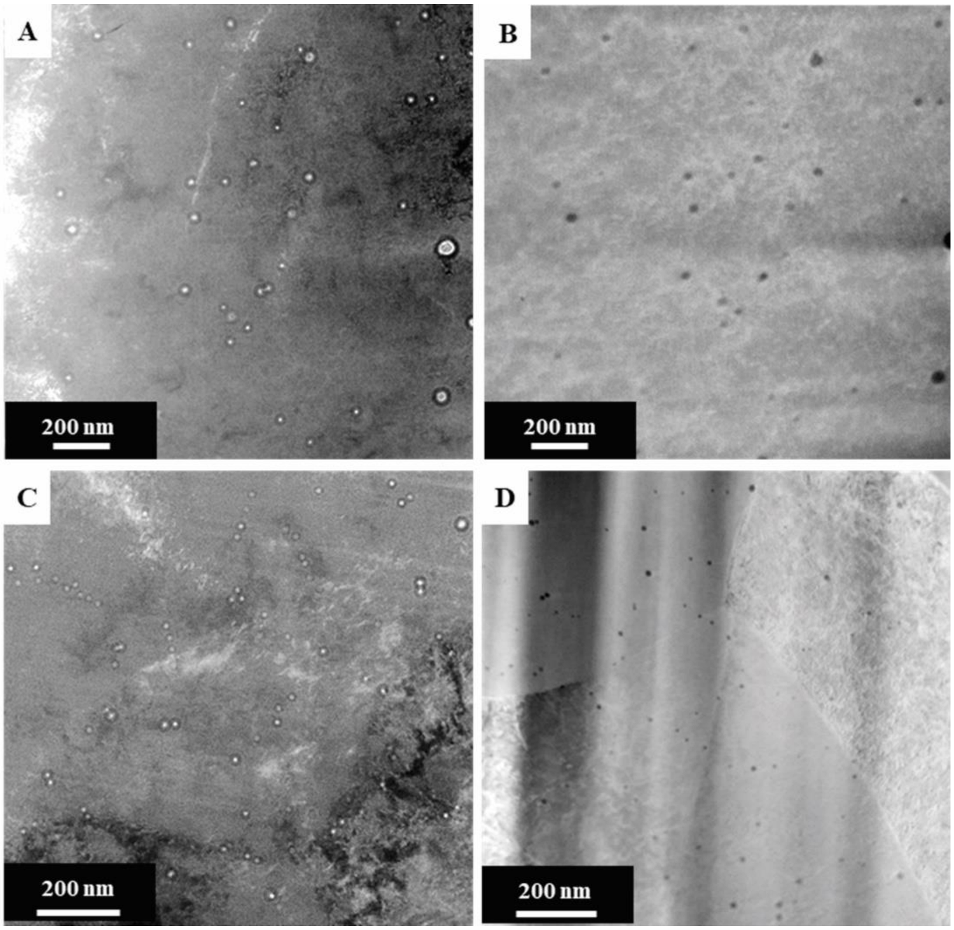

Figure 3.2.3. Under-focused BF-TEM and STEM-HAADF images of F/MA microstructures (type 2 cells) in alloy 1 produced by (AB) LPBF and (CD) SQ.

TEM foils of F/MA and PF microstructures (both type 2 cell) from SQ samples of alloys 1-3 showed no observable change in the sub-microscale structure and features with respect to change in composition or phase (F/MA or PF). In the BF and STEM-HAADF images of alloy 2 (Figure 3.2.4A-B) and alloy 3 (Figure 3.2.4C-D) no dislocation pileup was observed along the cell boundaries similar to in alloy 1. The oxide network that formed along the cell boundaries was the primary method of identifying the cellular structure. Still, the BF images needed to be under-focused to make the oxide network readily visible. The size range of oxides observed in alloys 2 and 3, like in alloy 1, ranged from ~5 to ~30 nm in diameter. No significant change was observed in the sub-microscale structure and features between the F/MA alloy 2 material and PF alloy 2 material.

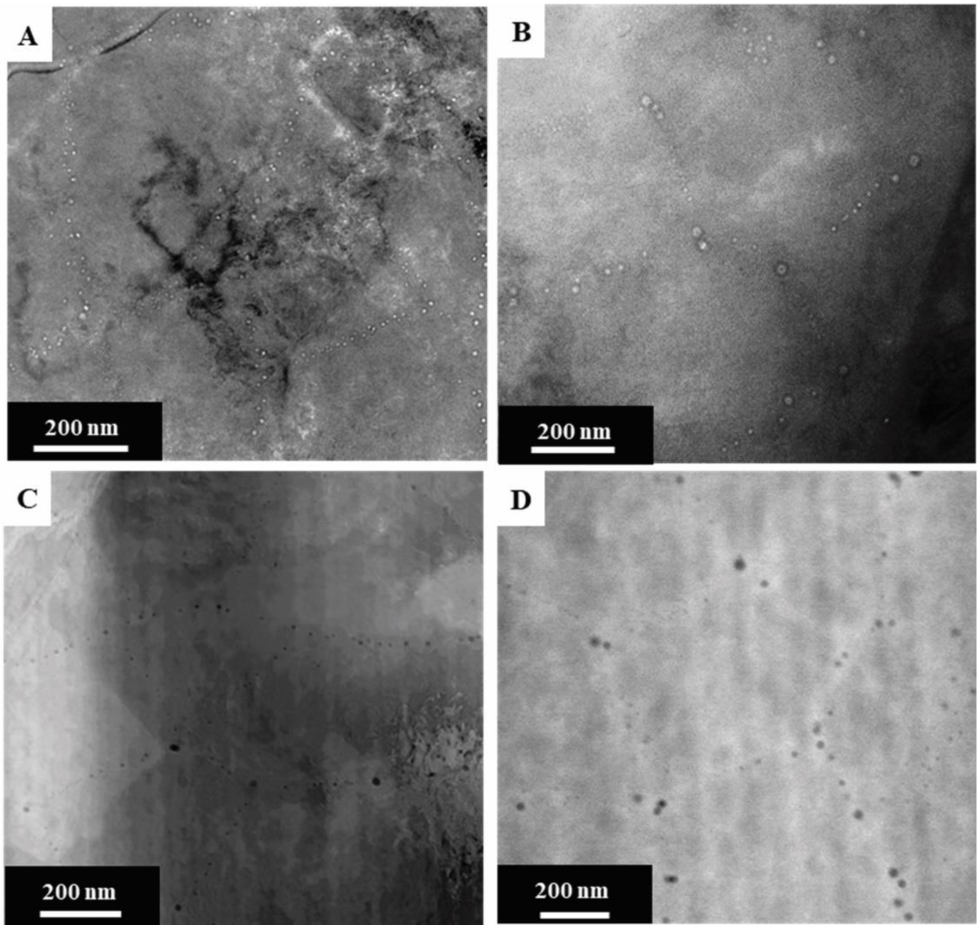

Figure 3.2.4. Under-focused BF-TEM and STEM-HAADF images of type 2 cells (ferrite solidification) from (A-B) the F/MA microstructure in SQ alloy 2 material and (C-D) the PF microstructure in SQ alloy 3 material.

3.3 STEM-EDX LPBF and SQ alloy 1.

STEM-EDX line scans of the PA microstructures produced by SQ and LPBF in alloy 1 revealed that Cr and Mo were the two main elements that segregated to the cell boundaries during austenite solidification. (Figure 3.3.1) Line profiles of the integrated and background subtracted signal intensities across solidification cells showed increased signal intensities for primarily Cr and Mo of the major alloying elements, and a decrease in Fe signal at the cell boundaries. This was observed in the STEM-EDX line profiles plotted in Figure 3.3.1 of PA cells from LPBF material (3.3.1A-C) and SQ material (3.3.1D-F). The red lines in Figures 3.3.1A and D represent the path that the line scans were collected over. Figures 3.3.1B and E are the integrated and background subtracted signal intensities of Fe, Cr, Ni, Mo, Mn, Si, and O from the line scan across the solidification cell marked in Figures 3.3.1A and D. Here the increase in Cr and Mo signal, as well as the decrease in Fe signal are visible, while the Ni signal shows no significant change in intensity at the cell boundaries. In Figure 3.3.1C and F, the ratio of signal intensities for Cr/Fe, Ni/Fe, and Mo/Fe are plotted for the same line. As mentioned in the methods section, a ratio of signal intensity vs Fe signal intensity was plotted to account for the changes in intensity resulting from changes in foil thickness. In Figures 3.3.1C and F, it is more easily observed that the intensity of Cr, Ni, and Mo remain stable throughout the body of the solidification cell. There was no observable change in signal intensity until the cell boundary was approached in which segregation is seen. The segregation of Cr and Mo in PA from both LPBF and SQ samples typically occurred within ~30nm on either side of the boundary. In the ratio of signal plot, the Cr/Fe, Ni/Fe, and Mo/Fe ratios were found to increase across the cell boundaries. This result differed from what was observed in the individual element signal intensities in which only Cr and Mo signal increased at the cell boundaries. The increase in Ni/Fe ratio was attributed to the decrease in Fe signal, not an increase in Ni. It was also observed that, in addition to increased Cr and Mo signal intensity at the cell boundaries, in some line scans, the intensity of the Mn and Si signals also increased. However, the increase in Mn and Si was not consistently observed and was not present in all line scans. There are a few potential explanations for this that are covered in the discussion section.

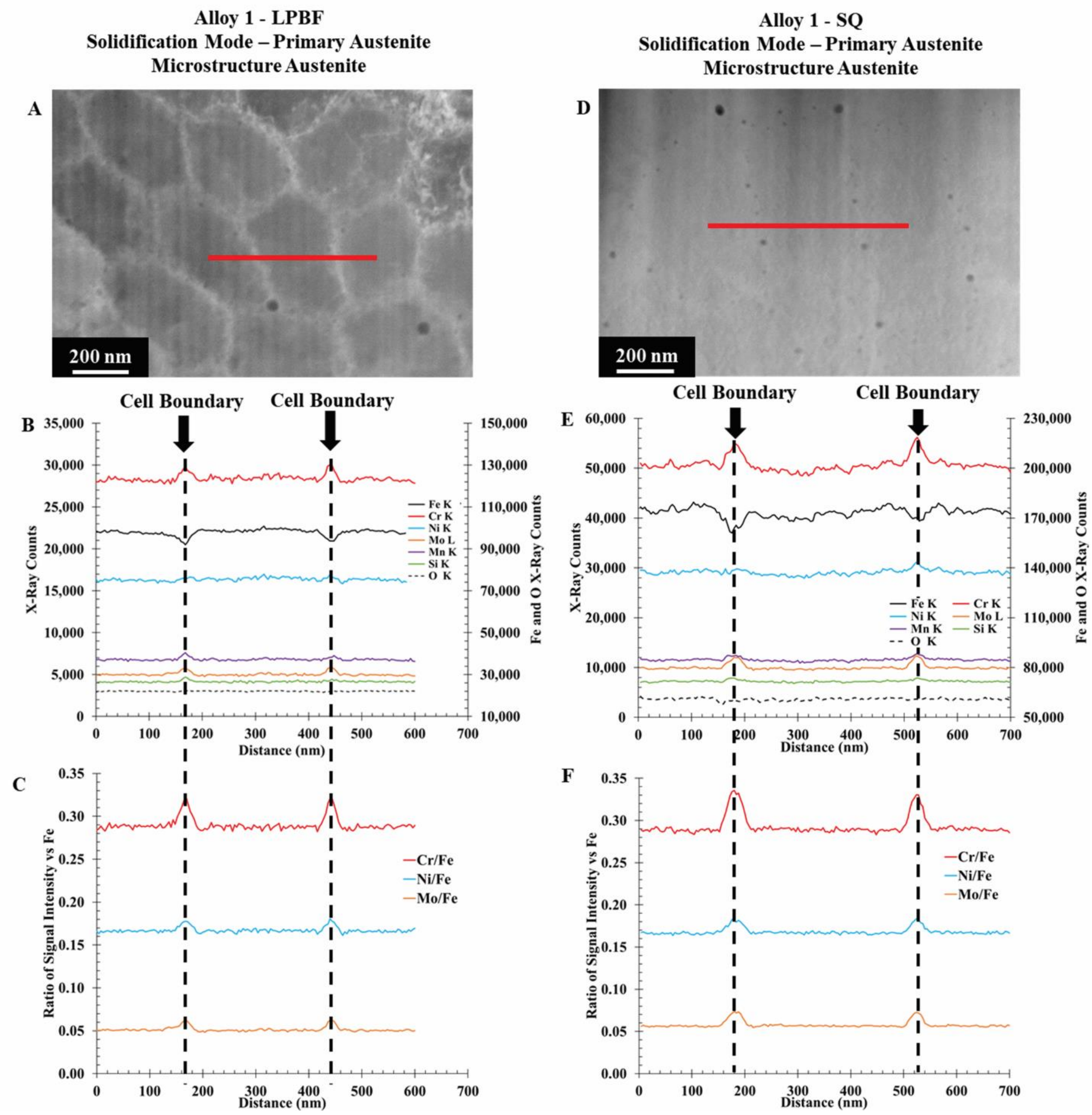

Figure 3.3.1. STEM-EDX line scans across a type 1 (austenite solidification) cells showing segregation of Cr and Mo to the cell boundaries in (A-C) LPBF and (D-F) SQ alloy 1 samples.

The F/MA microstructures produced by LPBF and SQ in alloy 1 were also very similar in segregation behavior in which Ni was the only observable element to segregate to the cell boundaries. Ni was the only element that experienced an increase in signal intensity across cell boundaries in the F/MA microstructures of LPBF and SQ samples. STEM-HAADF images with line scan locations indicated, signal intensity plots, and the ratio of signal intensity vs Fe plots from both line scans are shown in Figure 3.3.2A-F for the F/MA microstructures. Similar to the PA microstructures, the signal intensity remained stable throughout the cell body and only began to change when the cell boundary was approached. Unlike the PA segregation, the decrease in Fe signal was not as intense, so there was no observed increase in Cr/Fe and Mo/Fe signals when the ratio of signal intensities was plotted. The large variation in X-ray counts seen in Figure 3.3.2E were caused by variations in the sample thickness that occurred during FIB thinning, also known as curtaining. The curtaining is visible in the STEM-HAADF image in Figure 3.3.2D. The effects of curtaining are eliminated when the signal intensity of each element was plotted in a ratio against the Fe signal intensity, Figure 3.3.2F. (Goldstein, et al., 2018) Ni segregation in F/MA occurred over a greater distance from the boundary in LPBF than SQ, typically 150-200 nm on either side of the cell boundary in LPBF and between 50-100 nm in SQ samples. Both of these distances are larger than what was observed for Cr and Mo in PA microstructures.

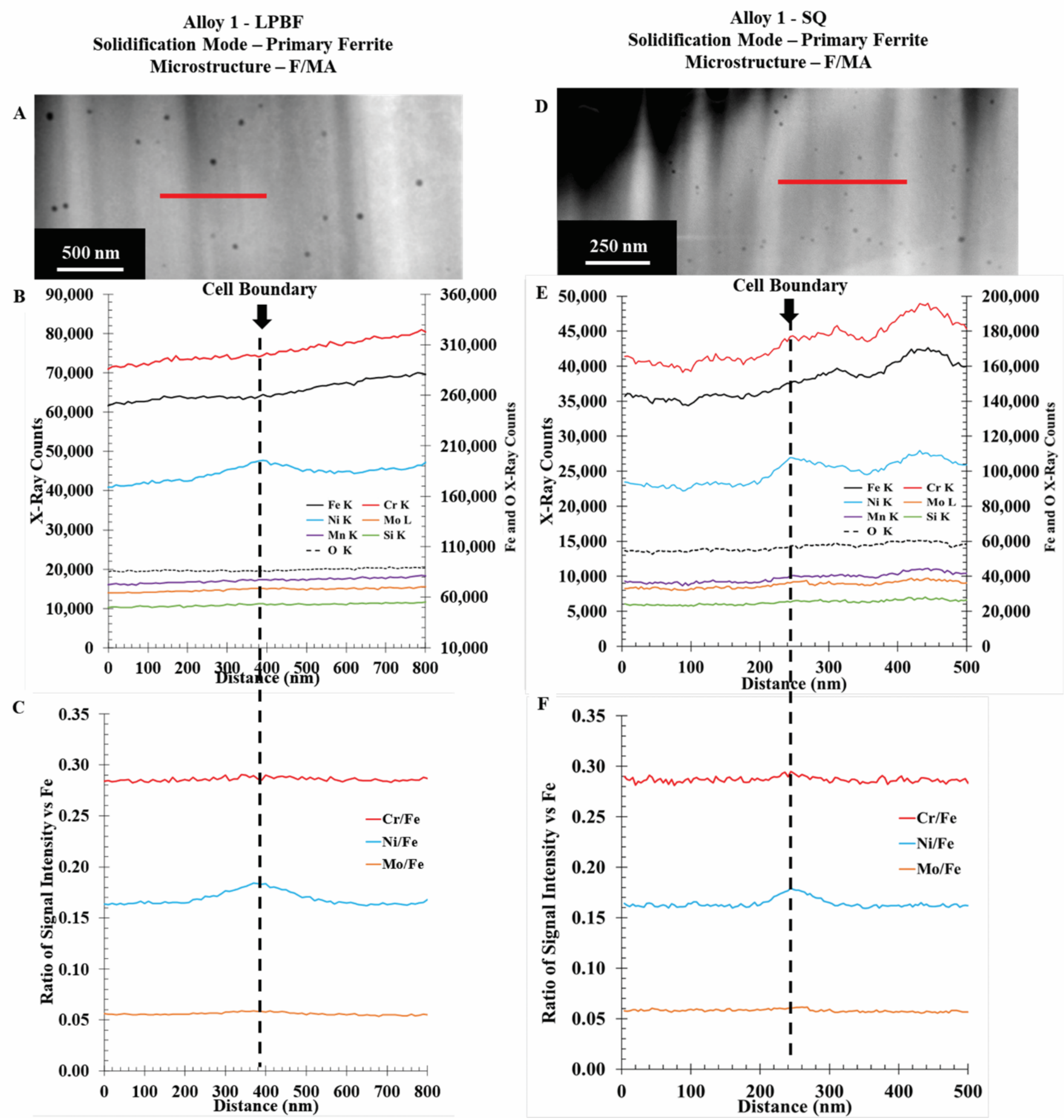

Figure 3.3.2. STEM-HAADF images and STEM-EDX line profiles from cell boundaries in the F/MA microstructure formed by the ferrite solidification mode for (A-C) LPBF alloy 1 material and (D-F) SQ alloy 1 material.

Using results from multiple STEM-EDX line scans, average segregation ratios were calculated to quantify the intensity of Cr, Ni, and Mo segregation in the PA and F/MA microstructures in LPBF and SQ processed alloy 1 samples. The average values and one standard deviation are listed in Table 3.3.1. In PA produced by LPBF and SQ, the segregation ratio for Cr and Mo were almost the same. The average value for Cr in LPBF was 0.94 ±0.01 and in SQ was 0.92 ±0.02. The segregation ratios for Mo in PA from LPBF and SQ were also close, at 0.84 ±0.01 and 0.82 ±0.03 respectively. The average segregation ratios and standard deviations for each element in PA for alloy 1 produced by LPBF and SQ are listed in Table 3.3.1A. The difference in the estimated average segregation ratios of Cr and Mo between LPBF and SQ were not large enough to be significantly different. The average segregation ratio of Ni in the PA microstructures from LPBF and SQ alloy 1 was 0.97 ±0.02 for both samples. While it is possible that a small amount of Ni segregation could be occurring, more extensive STEM-EDX analysis is required to confirm.

In LPBF and SQ produced F/MA microstructures from alloy 1, Ni was the only observed element to segregate to the cell boundaries. The average segregation ratios of Cr in the F/MA microstructures were near or equal to 1.00, indicating no meaningful segregation of Cr occurred. The segregation ratio of Mo in F/MA was slightly lower than 1.00 at 0.97 ±0.02. Similar to Ni in PA, whether a small amount of Mo segregation occurred or not can not be determined from the current data. Table 3.3.1B lists the average segregation ratios calculated for each element in the F/MA microstructures. Unlike in PA, the average segregation ratios of Mn and Si in F/MA were much closer to 1.00 for both LPBF and SQ sample. Possible causes for the difference of Mn and

Si segregation ratios between PA and F/MA microstructures will be addressed in the discussion section.

Table 3.3.1. Average segregation ratio estimates from STEM-EDX data with one standard deviation in (A) PA and (B) F/MA microstructures from LPBF and SQ alloy 1. Green bar represents primary segregating element in the respective microstructure.

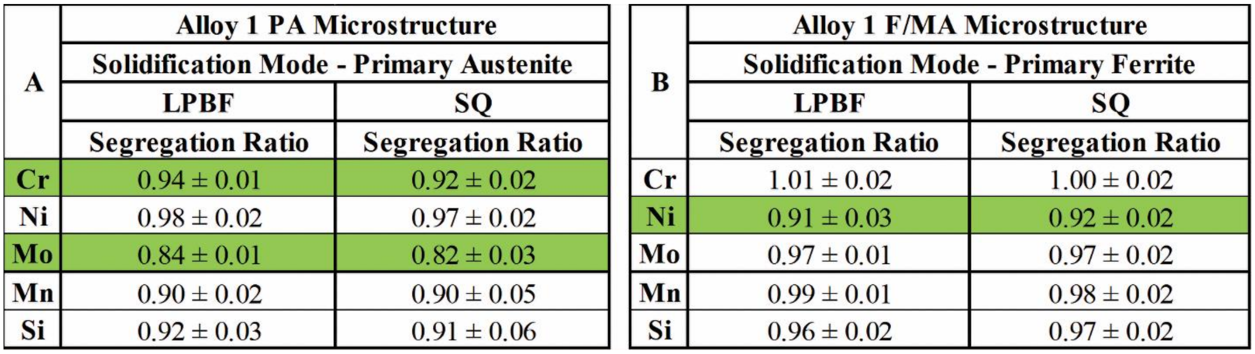

A	Alloy 1 PA Microstructure	
	Solidification Mode - Primary Austenite	
	LPBF	SQ
	Segregation Ratio	Segregation Ratio
Cr	0.94 ± 0.01	0.92 ± 0.02
Ni	0.98 ± 0.02	0.97 ± 0.02
Mo	0.84 ± 0.01	0.82 ± 0.03
Mn	0.90 ± 0.02	0.90 ± 0.05
Si	0.92 ± 0.03	0.91 ± 0.06

B	Alloy 1 F/MA Microstructure	
	Solidification Mode - Primary Ferrite	
	LPBF	SQ
	Segregation Ratio	Segregation Ratio
Cr	1.01 ± 0.02	1.00 ± 0.02
Ni	0.91 ± 0.03	0.92 ± 0.02
Mo	0.97 ± 0.01	0.97 ± 0.02
Mn	0.99 ± 0.01	0.98 ± 0.02
Si	0.96 ± 0.02	0.97 ± 0.02

3.4 STEM-EDX SQ alloy 1-3.

STEM-EDX data from the F/MA microstructure of SQ alloy 2 and PF microstructure of alloy 3 produced very similar segregation profiles as in F/MA from LPBF and SQ alloy 1. Again, Ni was the only element observed to segregate to the cell boundaries during solidification in the F/MA and PF microstructures. The signal intensity remained stable throughout the body of the cell until approaching the cell boundary. The distance from the cell boundary that Ni segregation occurred was similar to what was observed in SQ alloy 1, between 50-100nm typically. Figure 3.4.1 presents line profiles from two different line scans of the PF microstructure from alloy 3. Figure 3.4.1A-C spans a complete solidification cell while Figure 3.4.1D-F shows a line scan across the cell boundary with significantly higher counts. In both of these line profiles the increase in Ni signal and decrease in Fe signal are visible across the cell boundaries. Line profiles of the ratio of signal intensity vs Fe in Figure 3.4.1C and F and show slight increases to the ratio of Cr/Fe and Mo/Fe as a result of the decrease in Fe, but significant increases in individual Cr or Mo signals were not seen. Figure 3.4.2A-D show representative line profiles using the ratio of signal intensity vs Fe for Cr, Ni and Mo in the F/MA and PF microstructures for each alloy.

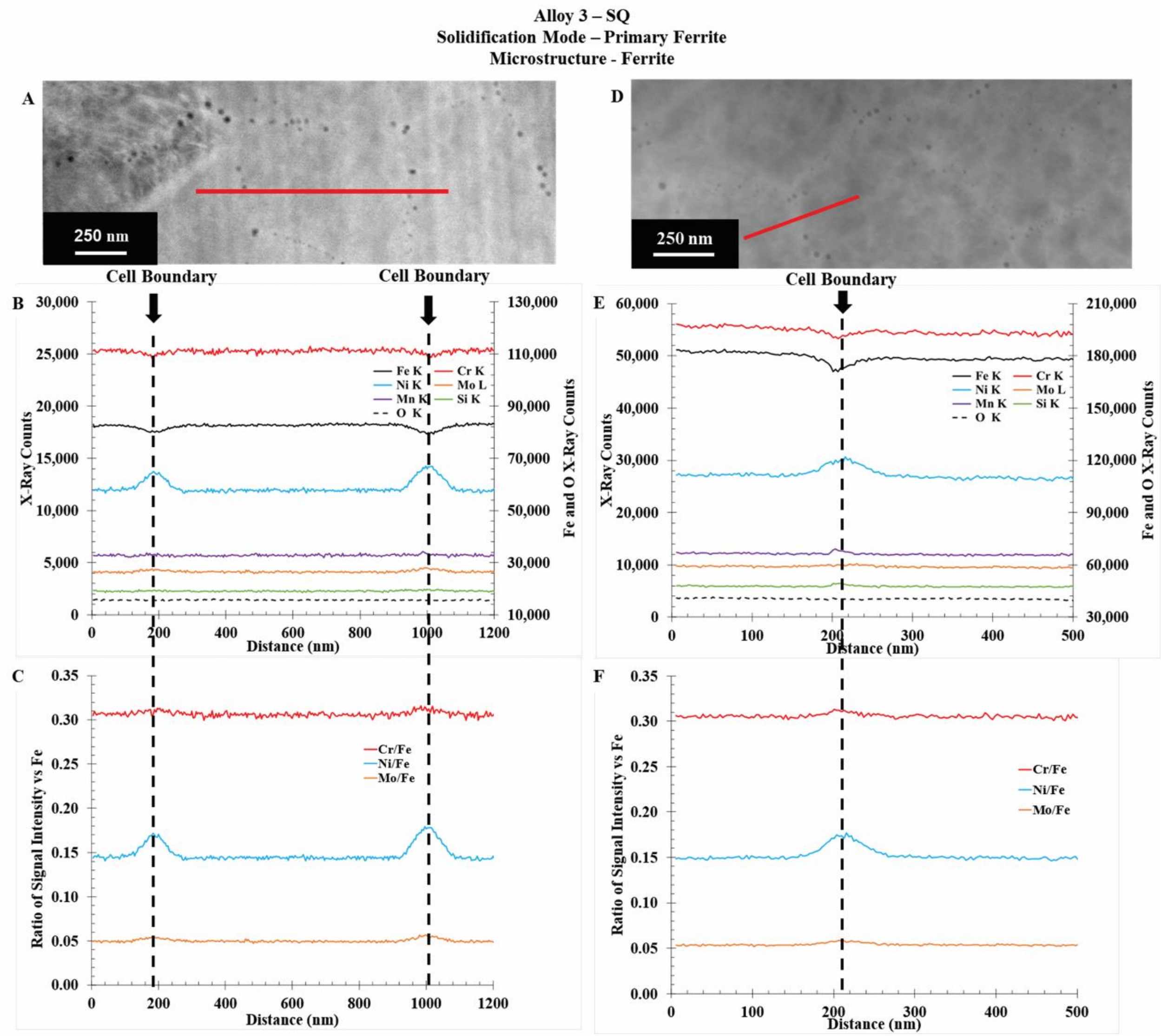

Figure 3.4.1. Line scan across two ferrite solidified, PF cell boundaries in SQ alloy 3. (A, D) STEM-HAADF images of in which the line scans were collected from, (B, E) integrated and background subtracted signal intensity line profile, and (C, F) ratio of signal intensity vs Fe line profile.

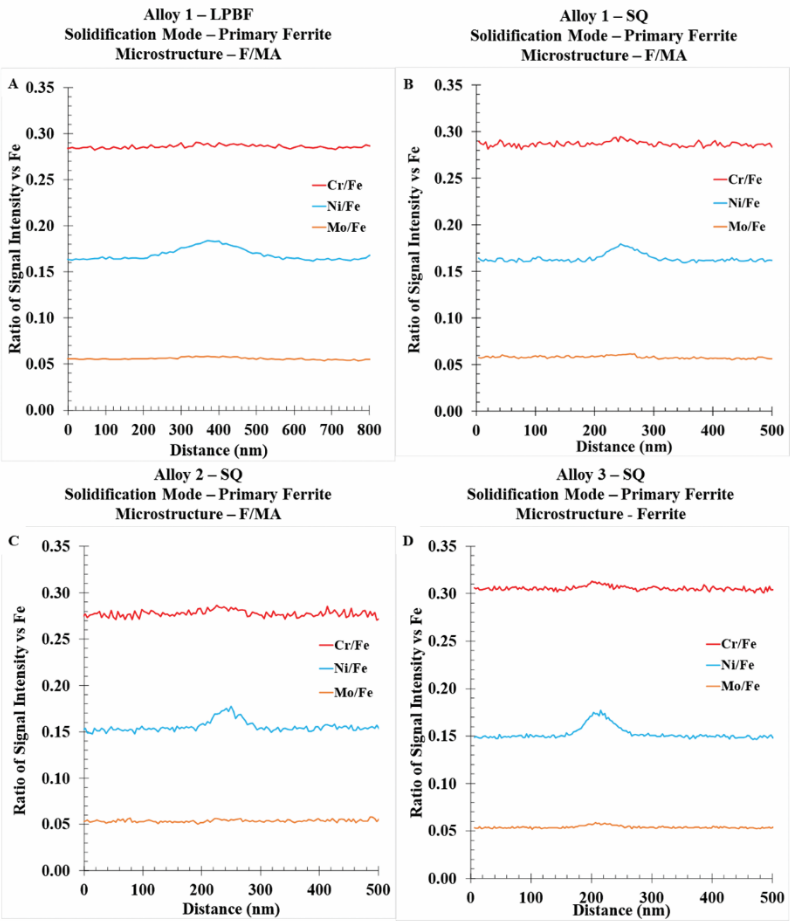

Figure 3.4.2. Line scan profiles using a ratio of signal intensities vs Fe signal intensity across cell boundaries in: (A) LPBF F/MA alloy 1, (B) SQ F/MA alloy 1, (C) SQ F/MA alloy 2, and (D) SQ PF alloy 3.

The average segregation ratios were calculated for the F/MA and PF microstructures in alloys 1-3 respectively, and when compared were found to be measurably indifferent regardless of microstructure, composition, or processing technique. The average segregation ratio of Cr was consistently at or near 1.00, while Mo, Mn, and Si ranged from 0.96-0.99 and although the average segregation ratio for these elements across microstructures/techniques were not identical, the differences between them were not significant. The only element with a segregation ratio significantly different from 1.00 in the F/MA and PF microstructures was Ni. The average segregation ratio ranged from 0.89-0.92. A direct comparison of the average segregation ratios for each microstructure condition can be found in Table 3.4.1. The segregation ratio of Ni in F/MA from LPBF was not measurably different from the values for Ni in the various SQ samples. Additionally, the average values of segregation ratios were not measurably different between the F/MA and PF microstructures or different alloy compositions.

Table 3.4.1. Average segregation ratio with one standard deviation for elements in F/MA microstructures in alloys 1 and 2, and PF in alloy 3. Green bar highlights primary segregating element in the respective microstructure.

	Alloy 1 F/MA Microstructure		**Alloy 2 F/MA Microstructure**	**Alloy 3 PF Microstructure**
	Solidification Mode - Primary Ferrite		**Solidification Mode - Primary Ferrite**	**Solidification Mode - Primary Ferrite**
	LPBF	**SQ**	**SQ**	**SQ**
	Segregation Ratio	**Segregation Ratio**	**Segregation Ratio**	**Segregation Ratio**
Cr	1.01 ± 0.02	1.00 ± 0.02	0.99 ± 0.03	1.01 ± 0.01
Ni	0.91 ± 0.03	0.92 ± 0.02	0.90 ± 0.04	0.89 ± 0.02
Mo	0.97 ± 0.01	0.97 ± 0.02	0.97 ± 0.02	0.96 ± 0.02
Mn	0.99 ± 0.01	0.98 ± 0.02	0.97 ± 0.04	0.99 ± 0.01
Si	0.96 ± 0.02	0.97 ± 0.02	0.98 ± 0.03	0.99 ± 0.02

3.5 STEM-EDX: Oxide particles.

STEM-EDX line scans across the oxide particles identified them as MnSi oxides in both the LPBF and SQ material. EDX line profiles collected across a single oxide particles from the PA microstructure in both the LPBF and SQ materials are shown in Figures 3.5.1A-B and C-D respectively. In both cases, the signal intensity decreased for Fe, Cr, Ni, and Mo while passing over the oxide and the Mn, Si, and O signals increased. In Figure 3.5.2, a higher magnification line scan of one of the larger oxide particles observed in LPBF material showed a similar increase in the Mn, Si, and O signals. Similar signal intensity responses were observed in both large and small oxide particles in each sample.

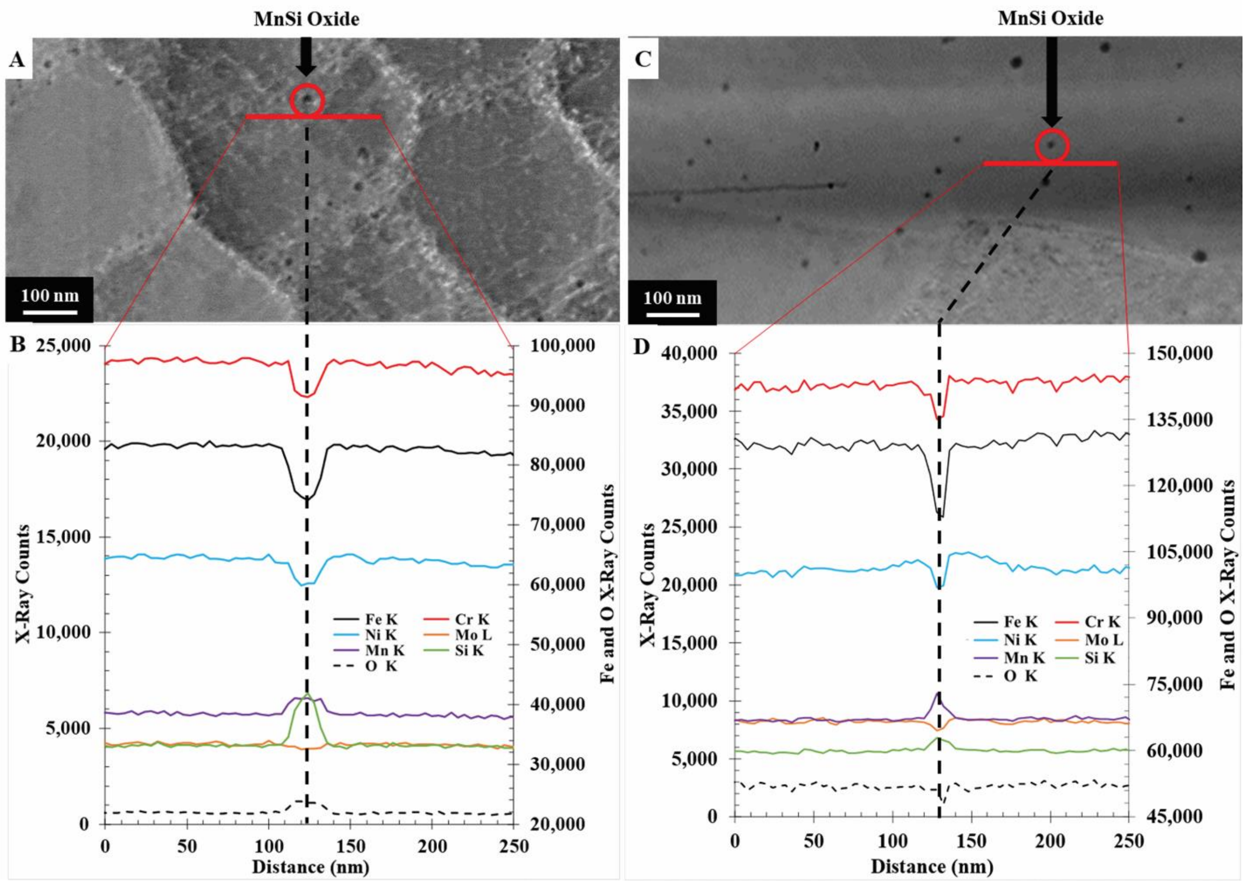

Figure 3.5.1. STEM-HAADF images and background subtracted, (AB) integrated signal intensity line profiles from a small oxide particle in LPBF alloy 1 material and (CD) in SQ alloy 1 material. Oxide particles are circled in red and the red lines indicating the path of the line scans are offset from the actual path of collection to keep the oxide particle visible.

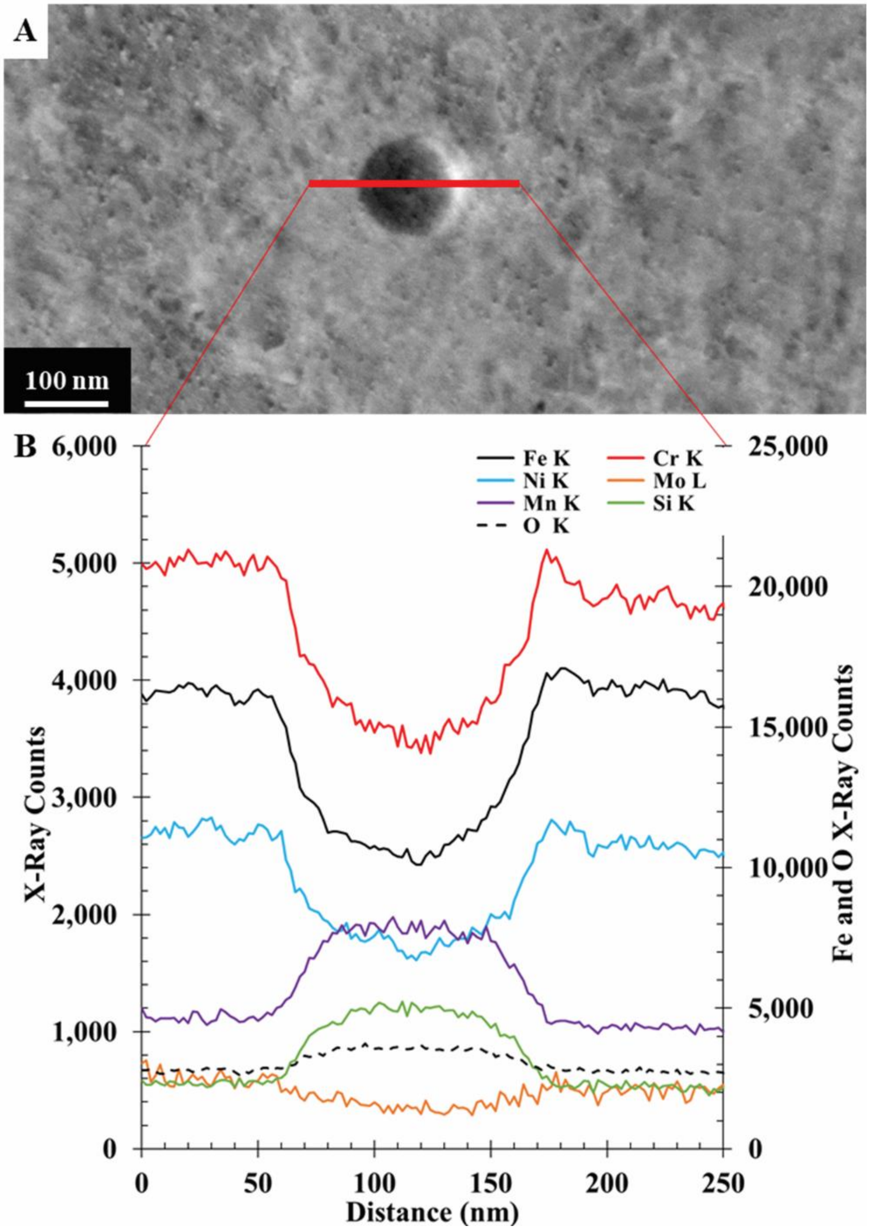

Figure 3.5.2. (A) STEM-EDX image and (B) signal intensity profile from line scan across large MnSi oxide from LPBF PA of alloy 1.

3.6 Thermodynamic simulations.

Thermodynamic simulation results were used to estimate the segregation ratio for individual elements in the primary solidification phases experienced in each alloy under multiple different solidification conditions. When using Scheil, as the system approaches complete solidification the final compositions become a function of how close to complete solidification the model is ran, meaning the solution can potentially greatly over or underpredict segregation. The simulations used in this work were stopped at 95% complete. The segregation ratios from classic Scheil solidification were the farthest from 1.0 of all simulations, predicting the most segregation for each element. The results from the Scheil with solute trapping module that were ran at 0.1m/s were the same as from the classic Scheil simulation results. This is due to the solidification rate not being fast enough to invoke solute trapping. When a 1m/s solidification rate was used, the model predicted less segregation shown by segregation ratio values closer to 1.0 for all elements. Lastly, at 5 m/s, even less segregation was predicted than in the 1m/s simulation with stabilizing elements (Cr and Mo in austenite solidification and Ni in ferrite solidification) approaching segregation ratios of 1.00. However, the segregation ratios predicted for the other elements were still farther from 1.00 than what was observed experimentally. (Table 3.6.1). The segregation ratios from simulations and experimental data for both solidification modes observed in alloys 1-3 are presented in Table 3.6.1A-D. In the PF solidification simulations, Table 3.6.1B-D, the segregation ratio values for Cr and Mo were found to be closer to what was observed experimentally than the values for Cr and Mo were in PA simulations. In general, the segregation ratios from simulations more closely matched the experimental estimates for elements that stabilized the primary solidification phase being simulated. (I.e., Ni in PA and Cr and Mo in PF) Additionally, although the values for Mn and Si showed greater deviation from the experimental values, this trend was still observed as the segregation ratio of Mn in PA simulations was closer to 1.00 than Si, and vice versa during PF simulations. The larger overall disagreement in Mn and Si was likely caused by the restriction of allowed phases to only liquid and the primary phase.

Table 3.6.1. Individual element segregation ratios calculated from Thermo-Calc solidification simulations using the Scheil module and Scheil with solute trapping module at 1m/s and 5m/s solidification rates compared with experimentally measured segregation ratios for the (A) PA solidification mode and (B-D) PF solidification mode for each alloy composition, alloy 1 - 3 respectively. Simulations were ran to 95% solidified. Experimental segregation ratios from Tables 3.3.1 and 3.4.1 with one standard deviation were included for reference.

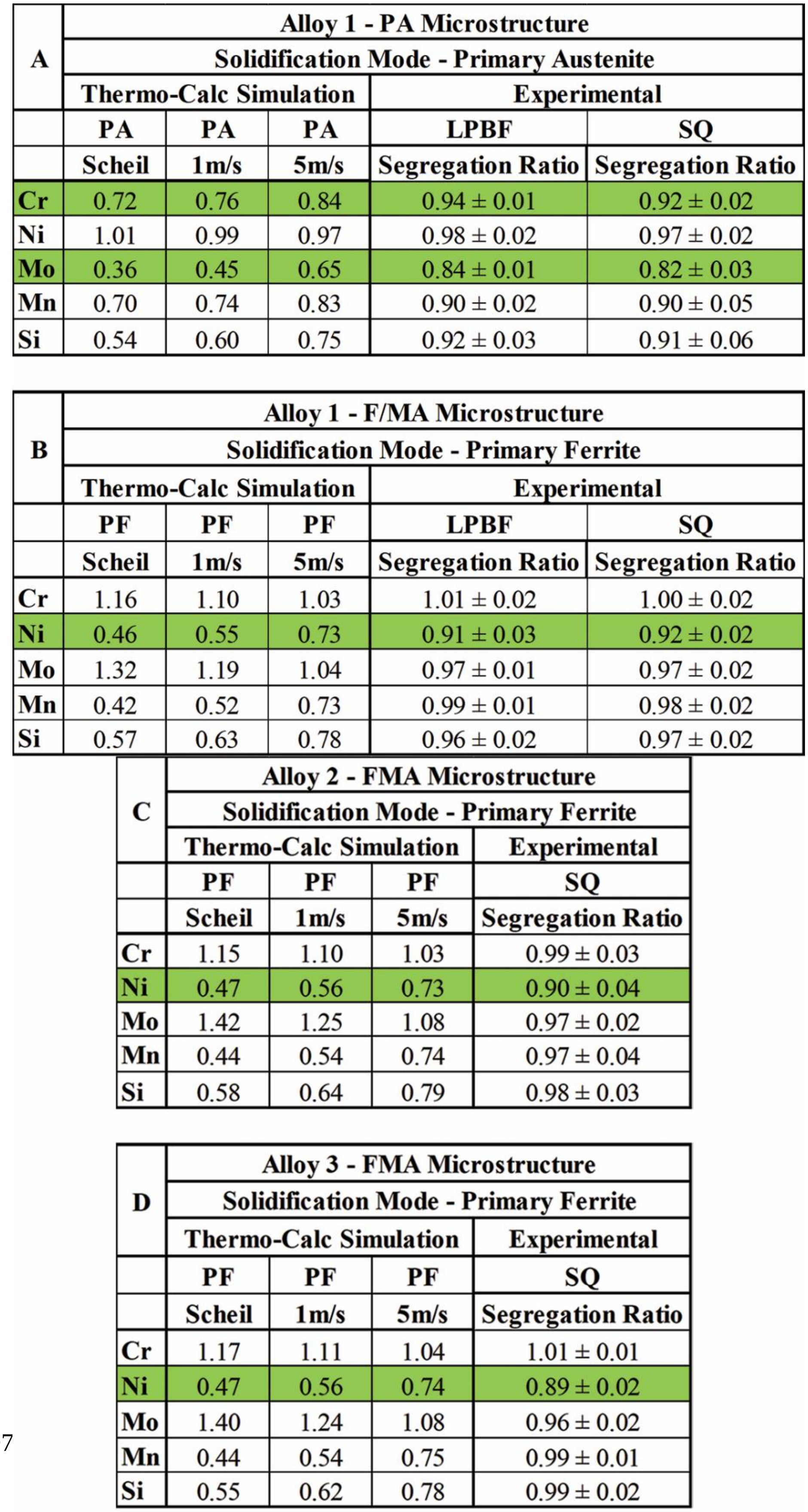

A	Alloy 1 - PA Microstructure				
	Solidification Mode - Primary Austenite				
	Thermo-Calc Simulation			Experimental	
	PA	PA	PA	LPBF	SQ
	Scheil	1m/s	5m/s	Segregation Ratio	Segregation Ratio
Cr	0.72	0.76	0.84	0.94 ± 0.01	0.92 ± 0.02
Ni	1.01	0.99	0.97	0.98 ± 0.02	0.97 ± 0.02
Mo	0.36	0.45	0.65	0.84 ± 0.01	0.82 ± 0.03
Mn	0.70	0.74	0.83	0.90 ± 0.02	0.90 ± 0.05
Si	0.54	0.60	0.75	0.92 ± 0.03	0.91 ± 0.06

B	Alloy 1 - F/MA Microstructure				
	Solidification Mode - Primary Ferrite				
	Thermo-Calc Simulation			Experimental	
	PF	PF	PF	LPBF	SQ
	Scheil	1m/s	5m/s	Segregation Ratio	Segregation Ratio
Cr	1.16	1.10	1.03	1.01 ± 0.02	1.00 ± 0.02
Ni	0.46	0.55	0.73	0.91 ± 0.03	0.92 ± 0.02
Mo	1.32	1.19	1.04	0.97 ± 0.01	0.97 ± 0.02
Mn	0.42	0.52	0.73	0.99 ± 0.01	0.98 ± 0.02
Si	0.57	0.63	0.78	0.96 ± 0.02	0.97 ± 0.02

C	Alloy 2 - FMA Microstructure			
	Solidification Mode - Primary Ferrite			
	Thermo-Calc Simulation			Experimental
	PF	PF	PF	SQ
	Scheil	1m/s	5m/s	Segregation Ratio
Cr	1.15	1.10	1.03	0.99 ± 0.03
Ni	0.47	0.56	0.73	0.90 ± 0.04
Mo	1.42	1.25	1.08	0.97 ± 0.02
Mn	0.44	0.54	0.74	0.97 ± 0.04
Si	0.58	0.64	0.79	0.98 ± 0.03

D	Alloy 3 - FMA Microstructure			
	Solidification Mode - Primary Ferrite			
	Thermo-Calc Simulation			Experimental
	PF	PF	PF	SQ
	Scheil	1m/s	5m/s	Segregation Ratio
Cr	1.17	1.11	1.04	1.01 ± 0.01
Ni	0.47	0.56	0.74	0.89 ± 0.02
Mo	1.40	1.24	1.08	0.96 ± 0.02
Mn	0.44	0.54	0.75	0.99 ± 0.01
Si	0.55	0.62	0.78	0.99 ± 0.02

4. Discussion

4.1 Comparison of LPBF and SQ samples.

Splat quenching process produced samples with very similar RS microstructures and sub-microscale features to LPBF processed samples of the same composition despite having different thermal histories during processing. It should be noted that the LPBF and SQ comparison presented here was for only a single composition (alloy 1). Although the processing techniques varied, the two samples produced microstructures that indexed as fully austenitic during EBSD analysis that were actually mixed microstructures consisting of both PA and F/MA. This was confirmed by the etched response, solidification structures, and elemental segregation observed in each. (Figures 3.1.1-2 and 3.3.1-2) The LPBF and SQ samples were morphologically different when observed after etching due to the different processing conditions. In LPBF, a laser is rastered across a thin layers of metal powder causing the loose powder to melt and resolidify as one piece. An overlapping raster pattern is typically used to melt and resolidify more loose powder with a portion of the previous melt pool. This results in at least part of the previously melted and solidified material to undergo the melt and solidification process multiple times. Additionally, while there are parts of the original melt pool that may only solidify once, there is a large amount of energy and heat being introduced to the solidified material from adjacent melt pools, and future layers. Thus, the bulk of the material will experience multiple heating and cooling cycles before cooling to room temperature once the build is complete. (Gorsse, et al., 2017; Sun, et al., 2016) Alternatively, in SQ samples are melted and solidified only once and only experience a single heating and cooling cycle before cooling to room temperature rapidly after solidification.

(Hayzelden, et al., 1982; Inokuti & Cantor, 1977) The two techniques also differ with respect to geometric constraints. In LPBF, heat is extracted primarily through contact with the previous melt pool/layer in which as in SQ, the liquid is in forced contact against the surface of the Cu platens during the splat event. Regardless of the differences in morphological appearances, earlier work demonstrated that the two techniques produced solidification cells over a range of sizes that primarily overlapped between 0.20 and 0.40 µm in diameter with similar solidification rate estimates between 0.4 and 0.8 m/s.

The sub-microscale structures and features of the PA and F/MA microstructures in both LPBF and SQ differed only slightly. During TEM analysis of the LPBF and SQ alloy 1 samples, regardless of whether the TEM foil contained the PA or F/MA microstructures, MnSi oxides of various sizes always formed along the cell boundaries. (Figures 3.2.1-3) The MnSi oxides ranged in size from 5-30nm in both the PA and F/MA microstructures for SQ material. However, in the LPBF material, the oxides formed over a larger size range from ~5 to ~100nm in diameter. (Figures 3.5.1-2) This size range is similar to the size ranges that have been previously reported for MnSi oxides in LPBF processed 316L. (Bajaj, et al., 2020; Deng, et al., 2020; Kong, et al., 2019a; Voisin, et al., 2021; Wang, et al., 2018) These oxides have been previously identified as $MnSiO_3$, Rhodonite. (Bajaj, et al., 2020; S. A. David, 1987; Voisin, et al., 2021; Voisin, et al., 2018; Wang, et al., 2018; Yan, et al., 2018) One possible explanation for the formation of larger oxide particles in the LPBF material compared to the SQ material has to do with the differences in thermal histories associated with each process. The material in LPBF undergoes multiple heating and cooling cycles before the finished part is complete while SQ is a single rapid solidification and cooling event. (DebRoy, et al., 2018) The longer period exposed to elevated temperatures would result in a higher mobility and promote a coarsening of the oxide particles. Work by F. Yan et. al. showed that when LPBF processed 316L was heat treated at 1200°C for 30 minutes the rhodonite particles increased in size. (Yan, et al., 2018) Additionally, differences in oxygen concentrations between LPBF and SQ alloy 1 samples are believed to not be responsible for the formation of larger oxide particles in LPBF material as the alloy 1 SQ experiments used LPBF processed alloy 1 material. As such, the alloy 1 SQ material started with the same levels of oxygen as the LPBF alloy 1, 0.04 wt%, but did not produce oxides of similar size. Also, the oxide size was consistent across SQ alloys 1-3 regardless of oxygen concentration.

The other difference was related to dislocation pile-up along cell boundaries in the PA microstructure. This feature has been reported previously in rapidly solidified austenitic 316L material processed via LPBF as a distinctive microstructure feature and would not necessarily be expected in the SQ material. (Bertoli, et al., 2019; Deng, et al., 2020; Voisin, et al., 2018; Wang, et al., 2018; Wilson, 2019) Dislocation pileup at the cell boundaries in LPBF is suggested to be caused by either oxide particles acting as Zener pinning sites for dislocations or segregation of elements such as Cr and Mo to cell boundaries having a pinning effect on dislocations. (Deng, et al., 2020; Lindroos, et al., 2022; Tucho, et al., 2018; Wang, et al., 2018; Yan, et al., 2018) During an LPBF build the material experiences repeated heating and cooling, and melting and resolidifying of the part causing non-uniform thermal expansion and contraction which would lead to lattice strain. (DebRoy, et al., 2018; Kong, et al., 2019a) Dislocations would be formed by the material in an attempt to accommodate and relax the lattice strain that built up during processing. Since SQ is a single thermal cycle technique there is less driving force for dislocations to be generated and could explain why dislocation pileup at the cell boundaries was not observed in the

SQ material. (Gao, et al., 2020; Sun, et al., 2016; Voisin, et al., 2021; Wang, et al., 2018; Yan, et al., 2019) Although, this does not explain the lack of dislocation networks in the F/MA microstructures of LPBF material. Two possible explainations for the lack of dislocations observed in the LPBF F/MA microstructure are either the ferrite crystal structure was unable to accommodate as many dislocations as the austenite structure or the dislocations were annihilated/relaxed during the solid-state transformation from ferrite to austenite due to the increase in lattice volume from ferrite to austenite, 0.68-0.74 respectivly. However, the current literature surrounding dislocation behavior during the ferrite to austenite massive transformations is sparse.

The elemental segregation observed in the PA microstructures showed Cr and Mo as the primary elements that segregated to the cell boundaries. (Figure 3.3.1) The segregation ratios that were calculated from this data represent the magnitude of segregation in Cr and Mo to cell boundaries and were not measurably different between LPBF and SQ samples. (Table 3.3.1) Similarly, in the F/MA microstructure, Ni was the only observed segregating element and the segregation ratios of Ni were not measurably different for the LPBF sample vs the SQ sample. (Figure 3.3.2, Table 3.3.1) In PA, the segregation ratio of Ni was estimated to be 0.97 ±0.02, not 1.00 even though Ni is an austenite stabilizer. In welding literature about segregation in austenitic 316L SS, Ni is regularly reported to segregate away from the dendrite/cell boundaries and be enriched at the dendrite/cell centers ($k>1.0$). (Brooks, et al., 1991; Kou, 2002) Based on the standard deviation and error from EDX collection a deviation of this size is not significantly large enough to be differentiated as significant segregation and while minor Ni segregation in rapidly solidified PA has been reported in previous studies of RS of 316L SS, it generally is not mentioned.

(Gorsse, et al., 2017; Voisin, et al., 2018; Wilson, 2019) Similarly, while segregation ratios of Mo in the F/MA and PF microstructures were 0.97 ±0.02 on average, Mo is a ferrite stabilizer and this small difference from 1.0 is not enough to be considered significant Mo segregation.

The segregation distance of Ni from the cell boundaries in F/MA microstructures of LPBF and F/MA and PF microstructures in SQ material were observably larger than the distance over which Cr and Mo segregated in PA microstructures. Additionally, the distance over which Ni segregated to the cell boundary in the LPBF material was larger the in the SQ material. One potential explanation for the larger distance over which segregation was observed could be caused by SSD during cooling. The presence of SSD of Ni in rapidly solidified ferritic microstructures has been previously proposed as reducing or eliminating the amount of segregation measured at the cell boundaries post solidification and cooling. (Brooks, et al., 1991; Iamboliev, et al., 2003; Wilson, 2019) Although both SQ and LPBF undergo rapid cooling rates on the order of 10^6-10^8 K/s, the amount of time required for solid-state diffusion at these length scales is estimated to be very small, between 1E-4 to 1E-6 seconds. The calculated diffusion distance for Cr and Ni in both austenite and ferrite can be found in Table 4.1.1. SSD would not be expected in a PA solidified microstructure because the diffusivity of elements in austenite is typically at least one order of magnitude smaller than in ferrite. (Battle & Pehlke, 1989; Brooks, et al., 1991; Elmer, et al., 1990; Moharil, et al., 1974) In austenite, the diffusion distances are almost negligible compared to the cell sizes, even at the slowest cooling rates, around 6 and 2 nm respectively. However, in ferrite, the SSD distance of Ni was estimated to be around 48-60 nm, while Cr was between 79-95 nm. The calculated SSD distances of Ni in ferrite supports the idea that both LPBF and SQ processed samples experienced some significant amount of SSD before transforming. Also, recall the average cell size in the LPBF material was larger than in the SQ material indicating slower cooling which would also allow for increased SSD in the LPBF material. While the diffusion distance of Ni in ferrite at slower cooling rates are larger, the difference is not larger enough to fully account for the larger distance over which Ni segregated in the cells in the F/MA LPBF material compared to the SQ samples. More in depth calculations or diffusion simulations could be used to further investigate these differences. In a direct comparison of the micro and sub-microscale structures and features same alloy processed using LPBF and SQ, the samples were similar with the three main differences being that: oxide particles in SQ microstructures did not form as large as in LPBF, dislocation pileup along the cell boundaries was observed in only the LPBF PA microstructure, and Ni segregation in the LPBF F/MA microstructure occurred over a greater distance from the cell boundaries than in SQ F/MA microstructures.

Table 4.1.1. Diffusion distance calculations for Cr and Ni in austenite and ferrite for three different potential durations before transformation temperature was reached.

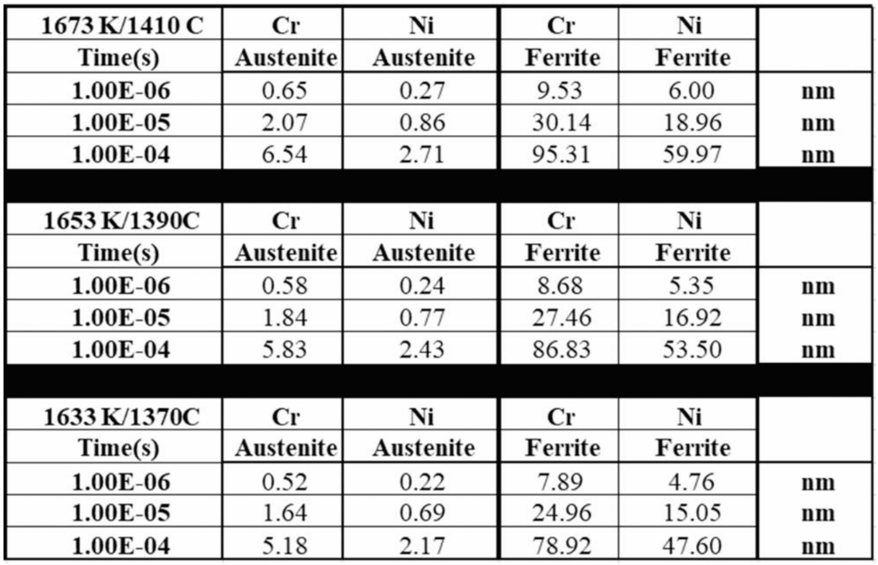

1673 K/1410 C	Cr	Ni	Cr	Ni	
Time(s)	Austenite	Austenite	Ferrite	Ferrite	
1.00E-06	0.65	0.27	9.53	6.00	nm
1.00E-05	2.07	0.86	30.14	18.96	nm
1.00E-04	6.54	2.71	95.31	59.97	nm

1653 K/1390C	Cr	Ni	Cr	Ni	
Time(s)	Austenite	Austenite	Ferrite	Ferrite	
1.00E-06	0.58	0.24	8.68	5.35	nm
1.00E-05	1.84	0.77	27.46	16.92	nm
1.00E-04	5.83	2.43	86.83	53.50	nm

1633 K/1370C	Cr	Ni	Cr	Ni	
Time(s)	Austenite	Austenite	Ferrite	Ferrite	
1.00E-06	0.52	0.22	7.89	4.76	nm
1.00E-05	1.64	0.69	24.96	15.05	nm
1.00E-04	5.18	2.17	78.92	47.60	nm

4.2 Comparison of SQ ferrite solidified microstructures with different Cr/Ni$_{eq}$.

The sub-microscale structures and features, and segregation in the two ferrite solidified microstructures (F/MA and PF) from SQ alloys 1, 2, and 3 were unaffected by changes in the Cr/Ni$_{eq}$ values. The three alloy compositions had Cr/Ni$_{eq}$ value of 1.53, 1.71, and 1.95 and all experienced at least partial ferrite solidification that resulted in either F/MA or PF as the final phase. (Figures 3.1.1 and 3.1.2) MnSi oxide particles formed a network that outlined the cellular solidification structures were observed in all both the F/MA and PF microstructures. The size of oxides that formed in each SQ sample was consistently between 5 and 30nm in diameter. (Figures 3.2.2-4 and 3.5.1-2). Additionally, although the three alloys had different concentrations of Ni, the magnitude of Ni segregation from ferrite solidification represented by the segregation ratio was found to not significantly differ. (Figure 3.4.1 and 3.4.2) From these results, it can be concluded that the amount of Ni segregation was not significantly affected by the targeted variations in Cr/Ni$_{eq}$ between the three different alloys, or the two microstructures formed by ferrite solidification.

The increases in the Mn and Si X-ray signals at cell boundaries in some line scans of PA from LPBF and SQ are likely not elemental segregation for a number of reasons. To begin with, the increase in Mn and Si signal at the cell boundaries was not present at all of the cell boundaries. Additionally, the increase in Mn signal could be caused by the increase in Cr signal at the cell boundary due to the overlap of the Cr kα and Mn kβ energy lines. This is supported by the lack of Mn and Si signal increase at the cell boundaries and segregation ratios in F/MA and PF microstructures. Another possible cause for the increase in Mn and Si signal is the presence of the MnSi oxides found along the cell boundaries and differentiating a signal increase from this vs segregation is difficult. Finally, it should be kept in mind that Mn is an austenite promoter and Si is a ferrite promoter, so the segregation of both elements in single phase would not be likely. It is for these reasons that the increases in Mn and Si signals observed across some cell boundaries in PA microstructures should not be considered to be from cellular segregation without further investigation.

4.3 Thermo-Calc solidification simulations.

Some potential causes for the differences between segregation ratio estimates from rapid solidification simulations and experimental results are due to the fraction solid value used in Scheil simulations or possible homogenization from SSD. The amount of segregation predicted by both classic and solute trapping Scheil solidification simulations was overestimated for most elements when compared to the experimental results. It is possible that for rapid solidification in LPBF and SQ, Scheil solidification will more accurately simulate the processes when solved to a lower amount of solidification rather than 95%. Also, these simulations were performed with only the liquid and primary solidification mode (austenite or ferrite) being allowed to form in order to achieve single phase solidification. Although the solidification rate estimates used for LPBF and SQ are below in which complete solute trapping is expected the observed increasing of segregation ratio values towards 1.00 for Ni in PA and Cr and Mo in PF are promising. Previous work in FBAM and laser welding discusses the possibility of cellular Ni segregation to be fully homogenized in PF as Ni does have a higher diffusion coefficient in ferrite compared to austenite.(Brooks, et al., 1991; Iamboliev, et al., 2003; Wilson, 2019) Similarly, the diffusion coefficients of Cr and Mo are also larger in ferrite vs austenite. Given the larger diffusion coefficients in ferrite, it could be suggested that after solidification there was sufficient SSD to homogenize Cr and Mo across the cell boundaries, but the greater amount of Ni segregation could not be completely homogenized and the amount observed experimentally is what remained. However, further investigation and modeling of potential SSD in the primary solidification phases in order to verify if this is the case.

5. Conclusions

In conclusion, this paper presents a detailed comparison between two rapid solidification (RS) processing techniques for austenitic stainless steel, two-piston splat quenching (SQ) and laser powder bed fusion (LPBF), to characterize and discuss the similarities and differences of various micro and sub-microscale features. Three alloys were used that had Cr/Ni$_{eq}$ ratios between 1.53

and 1.95 and spanned most of the composition space of the AISI A240 spec for 316L stainless steel. The results found that LPBF and SQ processing techniques produced very similar material in terms of elemental segregation, solidification morphology, oxide particles, microstructure, and sub-microscale structures and features. Extensive electron microscopy and EDX analysis, as well as computational thermodynamic modeling were used to estimate individual element segregation ratios in austenite and ferrite solidification. In this research we have noted the following:

1. Splat quench (SQ) processing of stainless steel material produced similar microscale and sub-microscale rapidly solidified features as those observed in the same material processed using laser powder bed fusion (LPBF). The size range of solidification cells that formed in both materials overlapped between 0.20 and 0.40 µm in diameter suggesting solidification rates between 0.4 and 0.8 m/s. Elemental segregation to the cell boundaries of Cr and Mo in PA and Ni in F/MA microstructures were mostly consistent between LPBF and SQ. Segregation ratio estimates from the segregation of Cr and Mo in PA were not measurably different between LPBF and SQ material, and the same was found for Ni in the F/MA microstructures. While the distance that Ni segregated to the cell boundaries in F/MA and PF were overall larger than Cr and Mo in PA, the distance was observably larger in LPBF than in SQ samples. This was possibly due to differences in thermal history allowing for greater SSD in the LPBF sample which is supported by solid-state diffusion calculations for Ni in ferrite. MnSi oxides formed along the cell boundaries in both microstructures ranging from 5-30 nm in SQ material and 5-100 nm in LPBF material. Also, dislocation pile-up along the cell boundaries was observed only in the LPBF PA microstructure.

2. Increasing the Cr/Ni_{eq} ratio over a range of 1.53 and 1.95 in SQ processed stainless steels did not notably change the sub-microscale features observed in the RS nanostructure. There was no significant change in the range of cell sizes in SQ microstructure of alloys with increased Cr/Ni_{eq} values. The size range of MnSi-rich oxides that formed in the SQ samples were not affected by the changes in Cr/Ni_{eq} or microstructure. The segregation of Cr and Mo, or Ni that occurred in each sample was controlled by the primary solidification phase (austenite or ferrite). The average segregation ratio of Ni in ferrite solidified SQ microstructures was found to not be measurably impacted by changes in the alloys Cr/Ni_{eq} ratio over a range of 1.53 to 1.95. Also, Ni segregation in F/MA microstructures was not measurably different from Ni segregation in PF microstructures.
3. Similar to as observed in the experimental results, segregation ratio estimates from rapid solidification simulations were not significantly impacted by changes in the alloys composition or Cr/Ni_{eq} ratio over a range of 1.53 to 1.95. Classic Scheil solidification predictions overestimated the amount of segregation that was observed in LPBF and SQ samples. The modified Scheil with solute trapping module produced segregation ratio values closer to experimental estimates, but even at higher solidification rates, were still farther from 1.00 than measured experimentally. This difference could be explained by SSD reducing the amount of segregation at the cell boundaries, but further investigation should be performed to confirm.

6. Acknowledgement

No resources from Framatome Inc. or Naval Nuclear Laboratories were used to perform the work reported or for the creation of this manuscript.

This work was funded by Honeywell Federal Manufacturing & Technologies under Contract No. DE-NA0002839 with the U.S. Department of Energy. The United States Government retains and the publisher, by accepting the article for publication, acknowledges that the United States Government retains a nonexclusive, paid up, irrevocable, world-wide license to publish or reproduce the published form of this manuscript, or allow others to do so, for the United States Government purposes.

REFERENCES

AKBARI, M. & KOVACEVIC, R. (2018). An investigation on mechanical and microstructural properties of 316LSi parts fabricated by a robotized laser/wire direct metal deposition system. Additive Manufacturing **23**, 487-497.

ASTM. (2020). ASTM A240 / A240M-20a Standard Specification for Chromium and Chromium-Nickel Stainless Steel Plate, Sheet, and Strip for Pressure Vessels and for General Applications. ASTM International.

AZIZ, M.J. (1982). Model for solute redistribution during rapid solidification. Journal of Applied Physics **53**(2), 1158-1168.

BAJAJ, P., HARIHARAN, A., KINI, A., KÜRNSTEINER, P., RAABE, D. & JÄGLE, E.A. (2020). Steels in additive manufacturing: A review of their microstructure and properties. Materials Science and Engineering: A **772**.

BARTOLOMEU, F., BUCIUMEANU, M., PINTO, E., ALVES, N., CARVALHO, O., SILVA, F.S. & MIRANDA, G. (2017). 316L stainless steel mechanical and tribological behavior—A comparison between selective laser melting, hot pressing and conventional casting. Additive Manufacturing **16**, 81-89.

BATTLE, T. & PEHLKE, R. (1989). Equillibrium Partition Coefficients in Iron-Based Alloys. Metallurgical Transactions: B **20**, 149-161.

BERTOLI, U.S., MACDONALD, B.E. & SCHOENUNG, J.M. (2019). Stability of cellular microstructure in laser powder bed fusion of 316L stainless steel. Materials Science and Engineering: A **739**, 109-117.

BOETTINGER, W.J., CORIELL, S.R. & SEKERKA, R.F. (1984). Mechanisms of microsegregation free solidification. Materials Science and Engineering **65**, 27-36.

BROOKS, J.A., BASKES, M.I. & GREULICH, F.A. (1991). Solidification Modeling and Solid-State Transformations in High-Energy Density Stainless Steel Welds. Metallurgical Transactions: A **22**, 915-922.

BROOKS, J.A. & THOMPSON, A.W. (1991). Microstructural development and solidification cracking suceptibility of austenitic stainless steel wels. International Materials Reviews **36**(1), 28.

CHERUVATHUR, S., LASS, E.A. & CAMPBELL, C.E. (2015). Additive Manufacturing of 17-4 PH Stainless Steel: Post-processing Heat Treatment to Achieve Uniform Reproducible Microstructure. JOM **68**(3), 930-942.

DEBROY, T., WEI, H.L., ZUBACK, J.S., MUKHERJEE, T., ELMER, J.W., MILEWSKI, J.O., BEESE, A.M., WILSON-HEID, A., DE, A. & ZHANG, W. (2018). Additive manufacturing of metallic components – Process, structure and properties. Progress in Materials Science **92**, 112-224.

DENG, P., YIN, H., SONG, M., LI, D., ZHENG, Y., PROROK, B.C. & LOU, X. (2020). On the Thermal Stability of Dislocation Cellular Structures in Additively Manufactured Austenitic Stainless Steels: Roles of Heavy Element Segregation and Stacking Fault Energy. JOM **72**(12), 4232-4243.

ELMER, J.W. (1988). The Influence of Cooling Rate on the Microstructure of Stainless Steel Alloys. In *Department of Materials Science and Engineering*, pp. 388. Massachusetts Institute of Technology.

ELMER, J.W. & EAGAR, T.W. (1988). Measuring the Residual Ferrite Content of Rapidly Solidified Stainless Steel Alloys. In *69th Annual AWS Meeting*, New Orleans: Welding Research Supplement.

ELMER, J.W., EAGAR, T.W. & ALLEN, S.M. (1989). Microstructural Development during Solidification of Stainless Steel Alloys. Metallurgical Transactions: A **20**, 2117-2132.

ELMER, J.W., EAGAR, T.W. & ALLEN, S.M. (1990). Single-Phase Solidification During Rapid-Resolidification of Stainless Steel Alloys. Weldability Mater.

GAO, S., HU, Z., DUCHAMP, M., KRISHNAN, P.S.S.R., TEKUMALLA, S., SONG, X. & SEITA, M. (2020). Recrystallization-based grain boundary engineering of 316L stainless steel produced via selective laser melting. Acta Materialia **200**, 366-377.

GOLDSTEIN, J., NEWBURY, D., MICHAEL, J., RITCHIE, N., SCOTT, J. & JOY, D. (2018). *Scanning Electron Microscopy and X-Ray Microanalysis*. Springer.

GORSSE, S., HUTCHINSON, C., GOUNE, M. & BANERJEE, R. (2017). Additive manufacturing of metals: a brief review of the characteristic microstructures and properties of steels, Ti-6Al-4V and high-entropy alloys. Sci Technol Adv Mater **18**(1), 584-610.

HAYZELDEN, C., RAYMENT, J.J. & CANTOR, B. (1982). Rapid Solidification Microstructures in Austenitic Fe-Ni Alloys. Acta Metallurgica.

IAMBOLIEV, T., KATAYAMA, S. & MATSUNAWA, A. (2003). Interpretation of Phase Formation in Austenitic Stainless Steel Welds. Welding Research Supplement, 337-348.

INOKUTI, Y. & CANTOR, B. (1977). The Formation Of Martensite In Splat-Quenched Fe-Mn and Fe-Ni-C Alloys. Journal of Materials Science **12**, 946-958.

J. A. SARREAL, G.J.A. (1986). The Effect of Solidification Rate on Microsegregation. Metallurgical Transactions: A **17**, 2063-2074.

JACOB, G. (2018). Prediction of Solidification Phases in Cr-Ni Stainless Steel Alloys Manufactured by Laser Based Powder Bed Fusion Process. NIST Advanced Manufacturing Series **14**, 38.

JONES, H. (1996). Cooling rates during rapid solidification from a chill surface. Materials Letters **26**, 133-136.

JONES, H. & SURYANARAYANA, C. (1973). Rapid Quenching From The Melt: An Annotated Bibliography 1958-72. Journal of Materials Science **B**, 705-753.

KATAYAMA, S. & MATSUNAWA, A. (1984). Solidification microstructure of laser welded stainless steels. In *International Congress on Applications of Lasers & Electro-Optics*, pp. 60-67.

KONG, D., DONG, C., NI, X. & LI, X. (2019a). Corrosion of metallic materials fabricated by selective laser melting. npj Materials Degradation **3**(1).

KONG, D., NI, X., DONG, C., ZHANG, L., MAN, C., CHENG, X. & LI, X. (2019b). Anisotropy in the microstructure and mechanical property for the bulk and porous 316L stainless steel fabricated via selective laser melting. Materials Letters **235**, 1-5.

KOTECKI, D.J. & SIEWERT, T.A. (1992). WRC-1992 Constitution Diagram for Stainless Steel Weld Metals: A Modification of the WRC-1988 Diagram. Welding Research Supplement, 171-178.

KOU, S. (2002). *Welding Metallurgy*. Wiley & Sons.

KÜRNSTEINER, P., WILMS, M.B., WEISHEIT, A., BARRIOBERO-VILA, P., JÄGLE, E.A. & RAABE, D. (2017). Massive nanoprecipitation in an Fe-19Ni- x Al maraging steel triggered by the intrinsic heat treatment during laser metal deposition. Acta Materialia **129**, 52-60.

KURZ, W. & FISHER, D.J. (1981). Dendrite Growth at the Limit of Stability: Tip Radius and Spacing. Acta Metallurgica **29**, 11-20.

KURZ, W., GIOVANOLA, B. & TRIVEDI, R. (1986). Theory of Microstructural Development During Rapid Solidification. Acta Metall. Mater. **34**, 823-830.

KURZ, W. & TRIVEDI, R. (1994). Rapid Solidification Processing and Microstructure Formation. Materials Science and Engineering: A **179/180**, 46-51.

LINDROOS, M., PINOMAA, T., AMMAR, K., LAUKKANEN, A., PROVATAS, N. & FOREST, S. (2022). Dislocation density in cellular rapid solidification using phase field modeling and crystal plasticity. International Journal of Plasticity **148**.

LIPPOLD, J.C. (1994). Solidification Behavior and Cracking Susceptibility of Pulsed-Laser Welds in Austenitic Stainless Steels. Welding Research Supplement, 129-140.

LIPPOLD, J.C. & SAVAGE, W.F. (1979). Solidification of Austenitic Stainless Steel Weldments: Part I-A Proposed Mechanism. In *AWS 60th Annual Meeting*, Detroit.

LIPPOLD, J.C. & SAVAGE, W.F. (1980). Solidification of austenitic SS weldments: Part II - The effect of alloy composition on ferrite morphology. In *AWS 60th Annual Meeting*, pp. 48-59. Detroit: Welding Research Supplement.

LIPTON, J., KURZ, W. & TRIVEDI, R. (1987). Rapid Dendrite Growth in Undercooled Alloys. Acta Metall. **35**(4), 957-964.

LIU, B.P.-H., CHUNG, T.-F., YANG, J.-R., FU, J., CHEN, C.-Y., WANG, S.-H., TSAI, M.-C. & HUANG, C.-Y. (2020). Microstructure Characterization of Massive Ferrite in Laser-Weldments of Interstitial-Free Steels. Metals **10**(7).

LIU, L., DING, Q., ZHONG, Y., ZOU, J., WU, J., CHIU, Y.-L., LI, J., ZHANG, Z., YU, Q. & SHEN, Z. (2018). Dislocation network in additive manufactured steel breaks strength–ductility trade-off. Materials Today **21**(4), 354-361.

MAS, F., TASSIN, C., ROCH, F., YESCAS, M., TODESCHINI, P. & BRÉCHET, Y. (2018). Growth Morphologies and Primary Solidification Modes in a Dissimilar Weld between a Low-Alloy Steel and an Austenitic Stainless Steel. Metals **8**(4).

MOHARIL, D.B., JIN, I. & PURDY, G.R. (1974). The Effect of d-Ferrite Formation on the Post-Solidification Homogenization of Alloy Steels. Metallurgical Transactions **5**, 59-61.

PRAKASH, U., BUCKLEY, R.A., JONES, H. & SELLARS, C.M. (1992). A Comparison Between Containerless Melting/Twin-Piston Splat Quenching and Chill-Block Melt Spinning as Techniques for Rapid Solidifcation of Late Transition Metal Aluminides. Materials Letters **14**, 274-277.

PREDECKI, P., MULLENDORE, A.W. & GRANT, N.J. (1965). A Study of the Splat Cooling Technique. Transactions of The Metallurgical Society of AIME **233**(8), 1581-1586.

QIU, C., KINDI, M.A., ALADAWI, A.S. & HATMI, I.A. (2018). A comprehensive study on microstructure and tensile behaviour of a selectively laser melted stainless steel. Sci Rep **8**(1), 7785.

QUINTANA, G., SIRKIN, H., ROSEN, M. & KURLAT, D. (1979). A Simple Splat-Cooling Equipment. Revista Brasileria de Fisica **9**, 123-128.

R. W. CAHN, K.D.K., M. LARIDJANI, M. GREENHOLZ, R. HILL. (1976). Novel Splat-Quenching Techniques and Methods for Assessing Their Performance. Materials Science and Engineering **23**, 83-86.

RUHL, R.C. (1967). Cooling Rates in Splat Cooling. Materials Science and Engineering **1**, 313-320.

RUHL, R.C. & COHEN, M. (1969). Splat quenching of iron-carbon alloys. Transactions of The Metallurgical Society of AIME **245**(2), 241-251.

S. A. DAVID, J.M.V., T. L. HEBBLE. (1987). Effect of Rapid Solidification on Stainless Steel Weld Metal Microstructures and Its Implications on the Schaeffler Diagram. Welding Research Supplement, 289-301.

SCHULZ, E.W. (2020). Short-Pulse Welding Technique for Resistance Spot Welding of Aluminum Alloy 6016-T4. In *Mechanical Eningeering*: The University of Alabama.

SCOTT, M.G. (1975). The Role of Melt Superheat in Splat-Quenching. Journal of Materials Science **10**, 269-273.

STEFANESCU, D. (2002). *Science and Engineering of Casting Solidification*. New York: Springer.

SUN, Z., TAN, X., TOR, S.B. & YEONG, W.Y. (2016). Selective laser melting of stainless steel 316L with low porosity and high build rates. Materials & Design **104**, 197-204.

TCHUINDJANG, J.T., SINNAEVE, M. & LECOMTE-BECKERS, J. (2017). Effects of High Solidification Rates on Segregations and Solid Phase Transformation in High Speed Steels. In *6th International Conference on Abrasion Wear Resistant Alloyed White Cast Iron for Rolling and Pulverizing Mills*.

THERMOCALC. (2021). Development of Non-Equilibrium Thermodynamic Tools for Additive Manufacturing.

TRIVEDI, R. & KURZ, W. (1994). Solidification Microstructures: A Conceptual Approach. Acta Metall. Mater. **42**, 15-23.

TRIVEDI, R., MAGININ, P. & KURZ, W. (1987). Theory of Eutectic Growth Under Rapid Solidification Conditions. Acta Metall. Mater. **35**, 971-980.

TUCHO, W.M., LYSNE, V.H., AUSTBØ, H., SJOLYST-KVERNELAND, A. & HANSEN, V. (2018). Investigation of effects of process parameters on microstructure and hardness of SLM manufactured SS316L. Journal of Alloys and Compounds **740**, 910-925.

VENKATARAMAN, S. (1984). Rapid solidification of stainless steels and FeAl ordered alloy by capacitor discharge welding. In *Materials Science and Engineering*: Madras University.

VOISIN, T., FORIEN, J., PERRON, A., AUBRY, S., BERTIN, N., SAMANTA, A., BAKER, A. & WANG, Y.M. (2021). New insights on cellular structures strengthening mechanisms and thermal stability of anaustenitic stainless steel fabricated by laser powder-bed-fusion. Acta Materialia **203**.

VOISIN, T., MCKEOWN, J., YE, J., CALTA, N., LI, Z., ROEHLING, T., DEPOND, P., SANTALA, M., CHEN, W., MATTHEWS, M. & M., W.Y. (2018). Deformation Mechanisms of SLM 316L Stainless Steel. Lawrence Livermore National Laboratory.

WANG, Y.M., VOISIN, T., MCKEOWN, J.T., YE, J., CALTA, N.P., LI, Z., ZENG, Z., ZHANG, Y., CHEN, W., ROEHLING, T.T., OTT, R.T., SANTALA, M.K., DEPOND, P.J., MATTHEWS, M.J., HAMZA, A.V. & ZHU, T. (2018). Additively manufactured hierarchical stainless steels with high strength and ductility. Nat Mater **17**(1), 63-71.

WILSON, D.M. (2019). Metallurgical and Mechanical Property Characterization of Additively Manufactured 304L Stainless Steel. In *Metallurgical and Materials Engineering*: Colorado School of Mines.

WOOD, J.V. & HONEYCOMBE, R.W.K. (1974). The Structure of Splat-Cooled Fe-20% Cr-25% Ni Austenitic Steel. Journal of Materials Science **9**, 1183-1189.

YAN, F., XIONG, W., FAIERSON, E. & OLSON, G.B. (2018). Characterization of nano-scale oxides in austenitic stainless steel processed by powder bed fusion. Scripta Materialia **155**, 104-108.

YAN, X., XU, X. & PAN, Q. (2019). Study on the Measurement of Stress in the Surface of Selective Laser Melting Forming Parts Based on the Critical Refraction Longitudinal Wave. Coatings **10**(1).

ZACHARIA, T., DAVID, S.A., VITEK, J.M. & DEBROY, T. (1989). Heat Transfer during Nd: Yag Pulsed Laser Welding and its Effect on Solidification Structure of Austenitic Stainless Steel. Metallurgical and Materials Transactions A **20A**, 957-967.